Article

Neuron

A Brain-wide Circuit Model of Heat-Evoked Swimming Behavior in Larval Zebrafish

Graphical Abstract

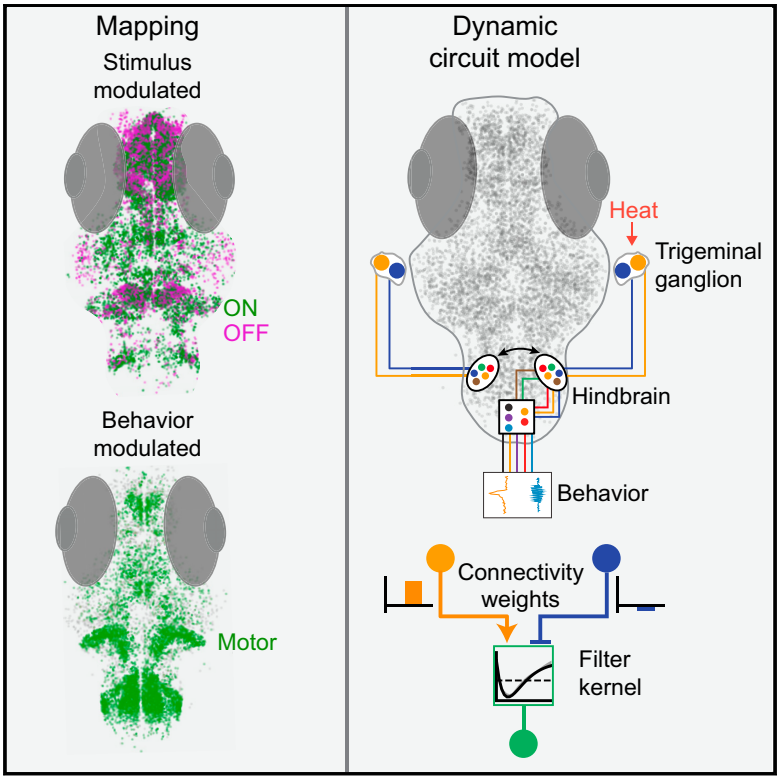

Highlights

- Temperature stimuli were combined with functional imaging and behavior recording
- Heat- and motor-encoding neurons were mapped throughout the larval zebrafish brain
- A critical transformation in heat representation was identified in the hindbrain
- A dynamic circuit model captures and quantifies the sensori-motor transformations

Authors

Martin Haesemeyer, Drew N. Robson, Jennifer M. Li, Alexander F. Schier, Florian Engert

Correspondence

haesemeyer@fas.harvard.edu (M.H.), schier@fas.harvard.edu (A.F.S.), florian@mcb.harvard.edu (F.E.)

In Brief

Haesemeyer et al. combine calcium imaging with behavioral recording and circuit modeling to reveal how temperature information is encoded and transformed in a vertebrate brain to generate behavior using a dynamic modeling strategy suited to capture temporal transformations in activity.

Haesemeyer et al., 2018, Neuron *98*, 1–15
May 16, 2018
https://doi.org/10.1016/j.neuron.2018.04.013

CellPress

Please cite this article in press as: Haesemeyer et al., A Brain-wide Circuit Model of Heat-Evoked Swimming Behavior in Larval Zebrafish, Neuron (2018), https://doi.org/10.1016/j.neuron.2018.04.013

Neuron
Article

A Brain-wide Circuit Model of Heat-Evoked Swimming Behavior in Larval Zebrafish

Martin Haesemeyer,[1,*] Drew N. Robson,[2] Jennifer M. Li,[2] Alexander F. Schier,[1,3,4,5,6,*] and Florian Engert[1,3,7,*]
[1]Department of Molecular and Cellular Biology, Harvard University, Cambridge, MA 02138, USA
[2]The Rowland Institute at Harvard, Cambridge, MA 02142, USA
[3]Center for Brain Science, Harvard University, Cambridge, MA 02138, USA
[4]Broad Institute of MIT and Harvard, Cambridge, MA 02142, USA
[5]Harvard Stem Cell Institute, Cambridge, MA 02138, USA
[6]Biozentrum, University of Basel, 4056 Basel, Switzerland
[7]Lead Contact
*Correspondence: haesemeyer@fas.harvard.edu (M.H.), schier@fas.harvard.edu (A.F.S.), florian@mcb.harvard.edu (F.E.)
https://doi.org/10.1016/j.neuron.2018.04.013

SUMMARY

Thermosensation provides crucial information, but how temperature representation is transformed from sensation to behavior is poorly understood. Here, we report a preparation that allows control of heat delivery to zebrafish larvae while monitoring motor output and imaging whole-brain calcium signals, thereby uncovering algorithmic and computational rules that couple dynamics of heat modulation, neural activity and swimming behavior. This approach identifies a critical step in the transformation of temperature representation between the sensory trigeminal ganglia and the hindbrain: A simple sustained trigeminal stimulus representation is transformed into a representation of absolute temperature as well as temperature changes in the hindbrain that explains the observed motor output. An activity constrained dynamic circuit model captures the most prominent aspects of these sensori-motor transformations and predicts both behavior and neural activity in response to novel heat stimuli. These findings provide the first algorithmic description of heat processing from sensory input to behavioral output.

INTRODUCTION

Environmental temperature strongly influences human behavior such as seeking shelter or wearing warm clothes in the cold. Similarly, most animal species have a narrow temperature range in which their metabolism functions optimally and have evolved behavioral strategies to seek out these preferred temperatures. Navigational strategies that lead animals to preferred temperatures within a heat gradient have been studied in diverse species, such as *E. coli*, *C. elegans*, zebrafish, and mouse (Hedgecock and Russell, 1975; Maeda et al., 1976; Murakami and Kinoshita, 1977).

At the molecular level, how animals sense temperature is well understood. A large group of transient receptor potential (Trp) channels are gated by temperature, and different Trp channels tile the temperature space from noxious cold to noxious heat (Caterina et al., 1997; Julius and Basbaum, 2001; Schepers and Ringkamp, 2010). In vertebrates, neurons expressing these channels are concentrated in the sensory trigeminal ganglia, innervating the face, as well as in the dorsal root ganglia, from which they detect stimuli across the trunk and tail (Erzurumlu et al., 2006; Schepers and Ringkamp, 2010).

Like other sensory stimuli, temperature has to be encoded and represented by neural activity in primary sensory neurons and subsequently needs to be filtered and processed to extract the information relevant for behavioral responses. Especially at the periphery, circuit studies have begun to elucidate how nervous systems encode temperature. For example, in *C. elegans*, the AFD neuron is specifically tuned to detect changes in temperature via response adaptation (Clark et al., 2006). This strategy is thought to provide information about temperature gradient direction aiding in navigation (Clark et al., 2007). In *Drosophila*, hot- and cold-sensitive neurons in the antenna form topographic projections in the brain (Gallio et al., 2011), and downstream thermosensory projection neurons that can be subdivided into "ON" and "OFF" classes have been implicated in heat avoidance behavior (Frank et al., 2015; Liu et al., 2015). In the mouse trigeminal ganglion, thermosensory neurons tile temperature space, with different neurons responding to different levels of cold or warmth (Yarmolinsky et al., 2016). Overall, most thermosensory neurons represent noxious temperatures, while encoding of ambient temperature is sparse (Yarmolinsky et al., 2016). Just like the aforementioned second-order projection neurons in *Drosophila*, second-order temperature-modulated neurons in the mouse spinal cord can be grouped into ON and OFF types (Ran et al., 2016). While warm-responsive neurons exclusively show sustained responses, cold-sensitive spinal cord neurons are generally fast adapting (Ran et al., 2016). Despite these advances at the cellular and molecular level, it remains unclear

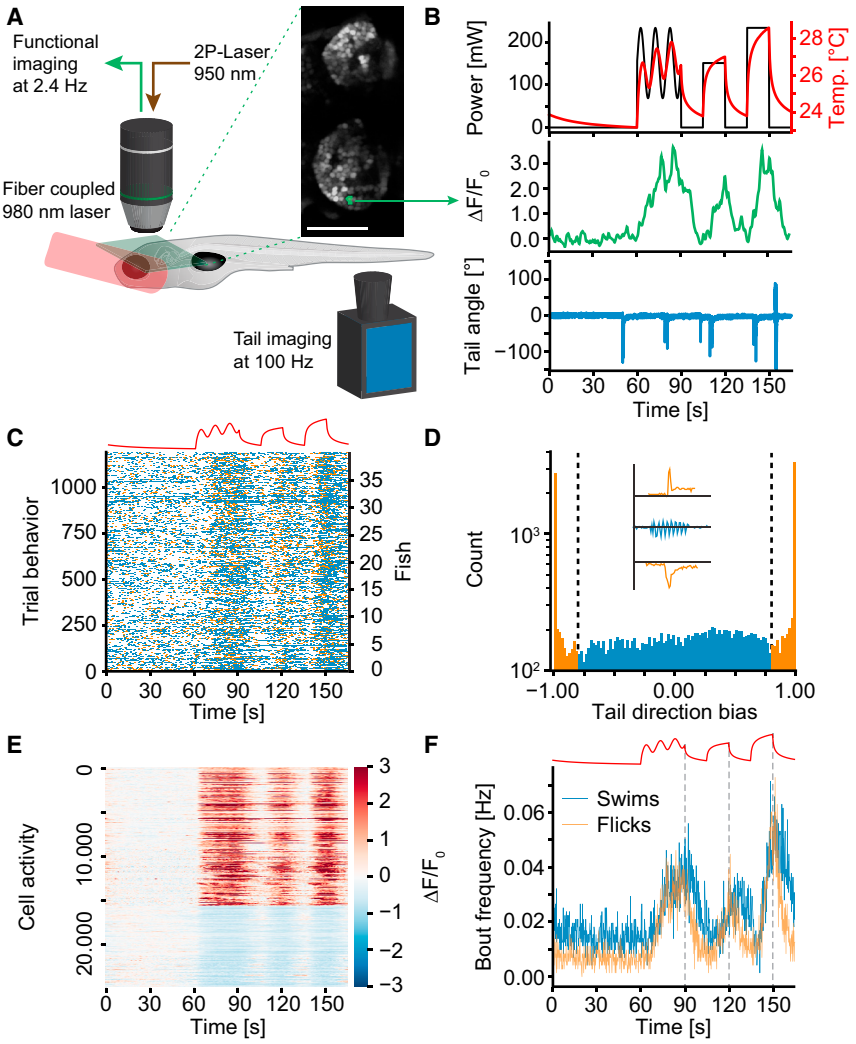

Figure 1. A Paradigm to Probe Heat Perception in Larval Zebrafish

(A) Setup schematic. Green plane depicts example imaging plane and inset shows habenulae imaged in one experiment. The activity of the green nucleus is depicted in (B).

(B) Top shows the delivered laser power in each repeat (black line) as well as the repeat-average temperature experienced by the fish (red line). Middle depicts repeat averaged calcium activity of one example ON cell. Bottom depicts example tail-trace during one repeat of one imaging plane.

(C) Behavior raster plot (summed across repeats) of 1,200 planes imaged across 40 fish. Blue ticks identify the start of swim bouts, orange ticks the start of flick bouts. Stimulus depicted on top for reference.

(D) Histogram of directional bias (see STAR Methods) of tail movement across all bouts in 40 fish. Coloring and dashed lines reflect cutoff between "flick" and "swim" categories. Inset shows example tail traces during flick to the left (top), swim (middle), and flick to the right (bottom).

(E) Heatmap of trial-averaged activity of all heat-responsive cells across all experiments. Cells are sorted according to ON versus OFF criteria. Color scale indicates ΔF/F0.

(F) Average bout frequencies of flick (orange line) and swim (blue line) type bouts. The stimulus is depicted on top for reference. Dashed gray lines indicate start of temperature decline to reveal off response in swims.

See also Figure S1.

how a temperature percept arises in the brain and how thermosensory activity ultimately leads to behavior. Thus, a description and analysis of the pathways that link temperature sensing to computational processes and behavioral outputs is lacking.

We recently investigated how temperature influences zebrafish swimming behavior. We found that zebrafish are sensitive to absolute levels as well as to changes in temperature and that different behavioral outputs—such as turning versus straight swims—are differentially influenced by ON- and OFF-responsive channels (Haesemeyer et al., 2015). In the current study, we establish brain-wide functional calcium imaging with heat stimulation and behavioral recording to identify heat processing centers throughout the larval zebrafish brain. We find that temperature information is represented in ON and OFF channels, and we identify different cell types that represent temperature on different timescales: some are slow modulated and others are fast adapting. In particular, cell types differ between anatomical regions, with the hindbrain favoring representation on faster timescales while some forebrain regions, including the preoptic area, represent temperature on longer timescales. Importantly, we identify a critical step in the sensori-motor transformations: trigeminal sensory neurons represent temperature exclusively using sustained ON and OFF cells, whereas activity diversifies in a trigeminal target area in the hindbrain. There, cell types with transient responses arise and form a more detailed representation of temperature stimulus features. Strikingly, this response type diversification is required to explain the behavior. We used these data to derive a realistic circuit model that captures the most important computations underlying the sensori-motor transformations. The circuit model not only captures neural activity transformations but also predicts behavior and neural activity in response to novel stimuli.

RESULTS

A System for Brain-wide Identification of Temperature-Encoding Cells

To observe neuronal activity and behavior in response to temperature stimuli, we used a fiber-coupled infrared laser delivering precise heat stimuli to a head-embedded larval zebrafish under a custom-built 2-photon microscope (Figures 1A and 1B). By freeing the tail of the larva, we could monitor behavior under infrared illumination at 100 Hz while simultaneously recording calcium activity at ~2.5 Hz.

Since changes in temperature led to expansion movements in our preparation, we developed an online z-stabilization technique that allowed imaging calcium responses without stimulus induced artifacts (Figures S1A–S1C). We imaged calcium activity in larval zebrafish pan-neuronally expressing the nuclear indicator H2B-GCaMP-6 s (Freeman et al., 2014). To study behavioral and neuronal heat responses, a heat stimulus consisting of both a sinusoidal temperature modulation and discrete temperature steps was presented to the larvae. We used a thermistor in place of the fish to calibrate our stimulus (Figure 1B; see STAR Methods). With a range of 24°C to 29°C, the heat stimulus stayed below the noxious temperature threshold of ~34°C. We probed each imaging plane with three stimulus trials and imaged 30 planes separated by 2.5 μm in each fish, achieving 3-fold coverage of the whole brain across 40 animals.

Across trials, the stimulus reliably induced behavior in all tested fish (Figure 1C). As seen in Figure 1B, larval zebrafish do not swim continuously but perform swim bouts at discrete intervals (Budick and O'Malley, 2000), and they can display bouts of different speeds and turn magnitudes. In our preparation, we noticed a prominent class of bouts that were characterized by unilateral flicks of the tail. We therefore used tail dynamics to divide the behavior into undulating "swims" and unilateral "flicks," which likely correspond to near-stationary turns in freely swimming behavior (Figure 1D). Importantly, larval zebrafish performed these two behaviors with different dynamics relative to the temperature stimulus. While flick and swim rates rose similarly as temperature increased, swim rates stayed elevated for a longer time after the temperature decreased (Figure 1F). This is likely part of an adaptive strategy, favoring straighter movements over in-place turns when temperature decreases.

We anatomically segmented individual cell nuclei and used spectral clustering (see STAR Methods) to extract stimulus-evoked activity in an unbiased manner across the whole brain. Imaging a total of 40 fish identified 24,947 responsive cells comprising around 4% of all imaged neurons. The neuronal responses broadly fell into two classes: ON-responsive cells, which are excited by increases in temperature, and OFF-type cells, which are inhibited by temperature or show rebound excitation when temperature decreases (Figures 1E and S1D–S1D''). Shuffling data with respect to the stimulus reduced the number of identified cells to fewer than 5% of the original set (Figure S1E). In control fish expressing an anatomical indicator (red fluorescent protein), our clustering approach did not reveal any fluorescence changes resembling our stimulus (Figures S1F and S1G).

To compare trial-to-trial variability across heat-modulated cells and behavior, we computed correlations between trial activity and behavior. While heat-modulated cells very reliably reported the stimulus with trial-to-trial correlations similar to a shot-noise model (Figure S1H), individual swim-bout generation was highly variable across trials (Figure S1I). Notably, behavioral variability across trials within fish was very similar to variability across fish (Figure S1I).

To compare activity and behavior across stimulus modalities, we imaged a second set of fish presenting a modified heat stimulus followed by an acoustic tap (Figures S1J–S1L). These taps elicited escape swims that were in most cases distinct from heat-induced unilateral flicks and generally classified as swims, consistent with their bilateral tail dynamics (Lacoste et al., 2015; Figure S1K). In summary, the head-embedded preparation enabled characterization of behavioral and neural dynamics across the whole brain while the animal was exposed to temperature and acoustic stimuli.

Heat-Related Activity Is Widespread but Anatomically Clustered throughout the Brain

Having established a preparation to monitor temperature-modulated neuronal activity, we set out to map heat processing centers throughout the larval zebrafish brain. To this end, we registered all imaging data onto a common reference brain (see STAR Methods; Portugues et al., 2014).

Neurons with heat-modulated activity could be identified throughout most of the brain prominently clustering in specific regions (Figures 2A–2D). In the sensory trigeminal ganglia, heat-sensing neurons occupied a specific caudal subdomain (Figure 2C, right insets) that was distinct from a more rostral location of tap-responsive cells identified in our heat and tap experiments (data not shown). In the hindbrain, heat cells formed a cluster in the dorsal cerebellum; another prominent cluster could be identified in rhombomeres 5/6 (Rh 5/6), which receive synaptic input from trigeminal fibers carrying information about aversive stimuli (Pan et al., 2012). The forebrain displayed widespread heat-related activity, with large fractions of heat-responsive cells in the sub-pallium as well as the right habenula (Figures 2A, 2B, and 2E). Furthermore, clusters of heat-responsive cells were identified in the pre-optic area, which has been implicated in temperature sensation and thermoregulation in mammals and reptiles (Cabanac et al., 1967; Dean and Boulant, 1989). Brain regions with heat-modulated activity generally contained both ON- and OFF-type cells with varying proportions (Figures 2C–2E), and with the exception of the cerebellum, most regions harbored more ON- than OFF-type cells.

After identifying heat-processing centers, we tested whether heat-modulated cells and their ON and OFF subtypes cluster in the brain or if they are instead distributed in a random manner. Comparing nearest-neighbor distances revealed that heat-modulated cells indeed clustered together and that this was maintained across subtypes such as ON and OFF cells as well (Figure S2A). This clustering indicates that functional subdivisions are reflected in the anatomical location of cell types. Notably, shuffling cell identities removed all region-specific cell and type clustering (Figures S2B–S2E). This confirms that the observed structure in the data is indeed a feature of the brain and does not simply arise by chance.

After the anatomical characterization, we wanted to know whether heat-modulated neurons likely encode heat information specifically or if some neurons generalize across modalities. To distinguish between these possibilities, we used the stimulus set combining temperature changes and aversive acoustic taps (Figure S1J) and identified cells that only respond to either the temperature or tap stimulus alone (unimodal cells) as well as cells that respond to both (multimodal cells) (Figure S2F). Importantly, the sensory trigeminal ganglia contained only unimodal cells for tap or for heat, a property which was also largely

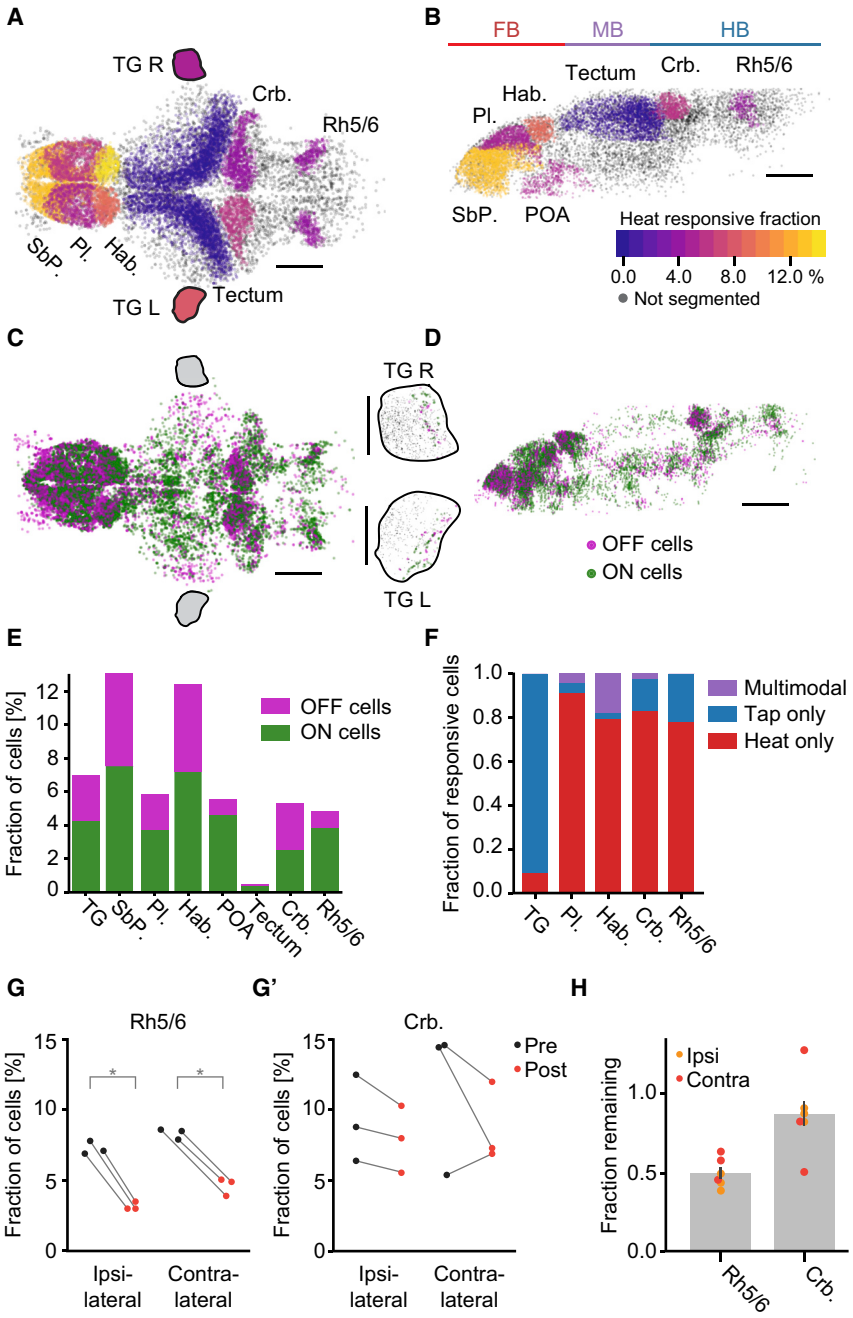

Figure 2. Heat-Related Activity Is Widespread across the Brain

(A and B) Fraction of heat-responsive cells within selected brain regions. Color scale indicates percentage of heat-sensitive cells within each region. Grey cells indicate brain regions that were not segmented. Scale bars, 100 μm. Pl.: pallium, SbP.: subpallium, Hab.: habenula, Crb.: cerebellum, Rh5/6: hindbrain rhombomeres 5 and 6, POA: preoptic area, TG L/R: left/right trigeminal ganglion. Colored lines on top delineate major subdivisions of the brain, FB: forebrain, MB: midbrain, HB: hindbrain. Note that trigeminal ganglia are not to scale.

(A) Dorsal view of the brain, anterior left, left side bottom.

(B) Side view of left hemisphere, anterior left, dorsal top.

(C) Distribution of ON (green) and OFF (magenta) cells across the zebrafish brain (top projection). The projection shows all cells identified across 30 individual experiments which have been registered onto a common reference brain. Scale bar, 100 μm, anterior left, left side bottom. Black outlines mark approximate location of trigeminal ganglia which are shown in insets to the right (TG L/R, left/right trigeminal ganglion). Each trigeminal ganglion depicts cells across five fish registered onto a common reference ganglion. Scale bar, 50 μm, anterior left.

(D) Side view of the brain in (C); only cells in the left hemisphere are depicted. Scale bar, 100 μm, anterior left, dorsal top.

(E) Fraction of heat ON cells (green) and heat OFF cells (magenta) in select brain regions.

(F) For regions that were imaged in heat and tap experiments, the fraction of stimulus-responsive cells that only responded to the heat stimulus (red), cells that only responded to the tap stimulus (blue) and multimodal cells that responded to both heat and tap (purple).

(G and G') Effect of ablating one trigeminal ganglion on the fraction of heat-responsive neurons in each brain hemisphere in Rh 5/6 (G) and the cerebellum (G') in three individual fish. Black dots show fraction of heat-responsive cells before and red dots after ablation. * = $p < 0.05$, rank-sum test.

(H) Fraction of pre-ablation heat-responsive cells remaining after ablation across Rh 5/6 and the cerebellum. Bar indicates average with bootstrap standard error across six hemispheres. Orange dots indicate ipsilateral effect, red dots indicate contralateral.

See also Figure S2.

reflected by cells in the hindbrain (Figure 2F, blue and red). While a much larger fraction of trigeminal cells responded to the strong tap stimulus than temperature, this distribution reversed in the hindbrain. Indeed, mechano-sensory *islet1*-expressing cells in the trigeminal do not form extensive arborizations in Rh 5/6, which could explain this difference (Pan et al., 2012). The forebrain, on the other hand, contained a significant fraction of multimodal cells, and taps were largely represented by these. Especially in the habenula, tap-responsive cells were almost exclusively multimodal, which suggests that taps are not encoded there with independent negative valence (Figure 2F).

To test the role of the trigeminal ganglia in temperature sensation, we imaged the hindbrain, subsequently ablated one trigeminal ganglion, and imaged the same region again. As expected, this unilateral ablation revealed a significant reduction in heat-modulated cells in Rh 5/6 (Figure 2G). Interestingly, even though the trigeminal ganglion only innervates the ipsilateral hindbrain (Pan et al., 2012), active cells were reduced both ipsilateral and contralateral to the ablation (Figure 2G). This indicates a crossing of information in the hindbrain. The reduction in the amount of heat-modulated cells in the cerebellum was smaller than in Rh 5/6 (Figures 2G' and 2H), which points to a non-linear

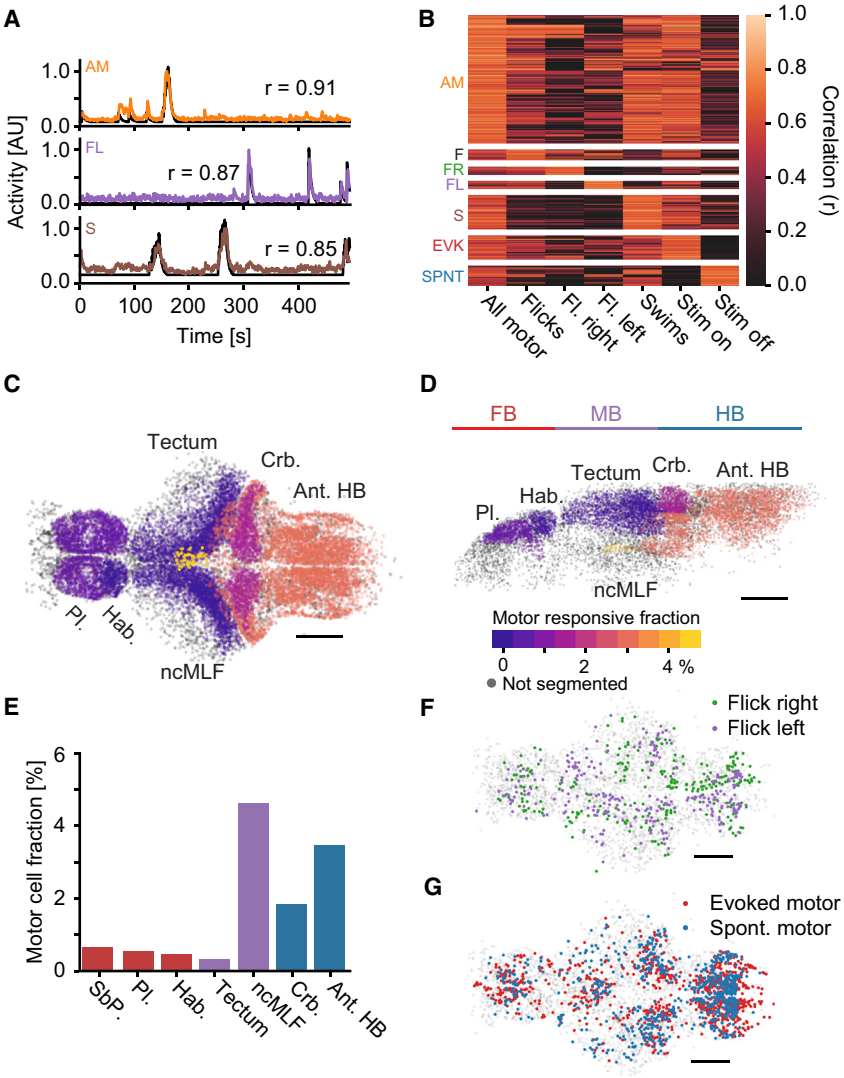

Figure 3. Motor Cells Can Be Separated According to Behavior and Stimulus Conditions

(A) Example behavioral regressors (black) and activity trace of one correlated cell. Top: Cell encoding all motor events in a plane (orange); middle: cell encoding left flicks in a plane (purple); bottom: cell encoding swims in a plane (brown). Numbers indicate correlation coefficient.

(B) Clustered heatmap of correlations of motor-cell activity with motor regressors, including the following events: All motor: all motor events of a given plane; Flicks: only flicks in a plane; Right/left flicks: only included right/left flicks; Swims: only swims included; Evoked motor: only motor events while the heat stimulus was on were included; Spontaneous motor: only motor events while the heat stimulus was off were included. Cells are only assigned to a more specialized motor cluster if the correlation to the specialized regressor is significantly higher than to the general regressor ($p < 0.01$, bootstrap hypothesis test). all-motor (AM): N = 5049 cells; flicks (F): N = 420; flick-right (FR): N = 319; flick-left (FL): N = 298; swims (S): N = 1338; evoked-motor (EVK): N = 950; spontaneous-motor (SPNT): N = 763. 30 fish.

(C and D) Fraction of motor correlated cells within selected brain regions. Color scale indicates percentage of motor-correlated cells within each region. Scale bars, 100 μm. Pl.: pallium, Hab.: habenula, ncMLF: nucleus of the medial longitudinal fascicle, Crb.: cerebellum, Ant. HB: anterior hindbrain. Grey cells indicate brain regions that were not segmented. (C) Dorsal view of the brain, anterior left, left side bottom; (D) side view of left hemisphere, anterior left, dorsal top.

(E) Quantification of percentage of motor correlated cells in select brain regions. Red bars: forebrain; purple: midbrain; blue: hindbrain.

(F) Distribution of flick-right (green) and flick-left (purple) cells, top projection. Anterior left, scale bar, 100 μm

G) Distribution of evoked-motor (red) and spontaneous-motor (blue) cells, top projection. Anterior left, scale bar, 100 μm.

Grey cells in (F)–(G) are non-motor-related cells representing brain outline.

See also Figure S3.

flow of sensory information through the hindbrain to the cerebellum and highlights a potential compensatory function of cerebellar circuitry.

In summary, the data demonstrate that heat-evoked activity is widespread throughout the brain, but heat-responsive neurons nonetheless cluster into specific regions such as the posterior trigeminal ganglion and rhombomeres 5 and 6 of the hindbrain or the cerebellum. Furthermore, while most neurons seem to be modality specific, especially in the forebrain, cell types arise that have a mixed representation of aversive stimuli.

Motor Cells Encode Swim Types and Are Stimulus Dependent

After pinpointing neurons and brain regions processing temperature stimuli, we sought to identify neurons with motor-correlated activity. To this end, we used the bout starts in each imaging plane (Figure 1C) to derive behavioral regressors by convolution with a calcium response kernel (Miri et al., 2011). These regressors represent the expected calcium response in a cell encoding the behavior and can therefore be used to probe the brain for cells showing activity that is strongly correlated ($r \geq 0.6$) to motor output (Figure 3A). Due to the high trial-to-trial variability of behavior (Figure S1I), these motor regressors are distinct from expected sensory responses; this large variability is also reflected in trial-to-trial variation of motor cell activity (Figure S1H).

We generated regressors encoding all motor events (Figure 3A, "AM") as well as regressors encoding the two subsets of motor events, flicks ("FL") and swims ("S"). Correlating activity across the whole brain to these regressors revealed a large representation of all motor events as well as neurons significantly more correlated to behavior-specific regressors such as either flicks to the right and left or swims (Figure 3B, $p < 0.01$, bootstrap hypothesis test).

Either motor events could be controlled by a single set of pre-motor cells or distinct stimulus modalities could influence different pre-motor pools. We therefore probed the brain for cells that encoded motor events in a stimulus-dependent manner. Namely, we created regressors that only reported motor output while the stimulus is being delivered or, conversely, during rest, while the stimulus is off. These regressors could indeed recover cells that encode behavior contingent on the stimulus presentation, either "evoked-motor" or "spontaneous-motor" cells (Figure 3B, "EVK" and "SPNT" respectively).

As expected, while "all-motor" cells were equally responsive during left and right flicks, "flick-left" and "flick-right" cells responded almost exclusively during left and right flicks, respectively (Figure S3A). Bout-triggered averages also revealed that "all-motor" cells respond with equal strength irrespective of the stimulus, while "evoked-motor" and "spontaneous-motor" cells showed a much stronger response in the presence or absence of the stimulus, respectively (Figure S3B). Shuffling the activity data with respect to the behavior reduced the number of identified cells to less than 1.8% (Figures S3C and S3D).

The anterior hindbrain and cerebellum contained prominent clusters of motor-related cells (Figures 3C, 3D, S3E, and S3F). Notably, the trigeminal ganglia also harbored a few motor-correlated cells in a rostral region mostly distinct from the caudal heat-sensitive domain (Figure S3E). We also identified a cluster of motor cells in the nucleus of the medial longitudinal fascicle (ncMLF), which has been implicated in controlling swim speed (Severi et al., 2014; Figures 3C and 3D). While a sizeable fraction of hindbrain and ncMLF neurons encoded motor behavior, there were only few such neurons in the forebrain (Figure 3E). Cells encoding flicks to the left versus right were notably absent from the ncMLF and showed a lateralized distribution in the hindbrain, where more cells encoded behavior in an ipsilateral manner (Figure 3F). Evoked-motor and spontaneous-motor cells, on the other hand, were largely dispersed throughout motor-related brain regions but did cluster spatially within those regions (Figure 3G).

In summary, behavioral subtypes and stimulus contingencies are encoded by separate pools of motor cells that are largely confined to regions previously described as encoding motor activity (Dunn et al., 2016; Naumann et al., 2016).

Activity Decorrelation in the Hindbrain Is Required to Explain Behavior

After the identification of heat- and motor-encoding cells in the brain, we wanted to know how well temperature-related activity in specific regions can explain the observed swim and flick behaviors. To this end, we partially annotated our reference brain with Z-Brain annotations (Randlett et al., 2015). This allowed extracting sensory-related activity using spectral clustering for cells in specific regions, effectively capturing more diversity than brain-wide clustering (see STAR Methods). This analysis revealed that stimulus representation in the sensory trigeminal neurons is simple, consisting of one ON and one OFF cell type tracking the stimulus with slow dynamics (Figure 4A). Furthermore, the activity of both cell types was highly anti-correlated (Figure 4A'), indicating that they have very similar stimulus encoding, albeit with opposite signs.

We next asked whether a simple linear regression model using the activity present in the trigeminal sensory ganglion could explain the observed flick and swim rates. Activity in the trigeminal was indeed sufficient to explain flick-type bout generation, capturing more than 90% of the variance in this behavior (Figure 4A'' left), but it was considerably worse in explaining swims, capturing less than 70% of the variance (Figure 4A'' right).

In the Rh 5/6 region of the hindbrain, a trigeminal target area (Pan et al., 2012), activity profiles became considerably more diverse with the presence of two distinct ON and three distinct OFF cell types (Figure 4B). Importantly, both transient "fast-ON" and transient "fast-OFF" activity arose in this region, while another set of "slow-ON" and "slow-OFF" neurons mostly reflected trigeminal activity (Figure 4B). These new response types change the stimulus representation from exclusively encoding temperature levels to also representing the direction of temperature change. The distinct temporal dynamics furthermore resulted in a decorrelation of activity at this first relay station (Figure 4B'). Remarkably, combining the activity of just two response types—the trigeminal-like slow-ON and a newly formed Fast-OFF type—was sufficient to explain both flick and swim behavior, capturing 90% of the variance in both behaviors (Figure 4B''). This suggests that the observed response diversification underlies the generation of behavior.

Analyzing activity in other brain regions revealed differences in stimulus representation throughout the brain (Figures S4A–S4E). Temperature-related activity in the cerebellum followed different dynamics than activity in Rh 5/6, and the representation of stimulus amplitude was strongly reduced in this region (Figure S4A). The forebrain, especially the pallium (Figure S4C) and pre-optic area (Figure S4E), contained activity types that evolve on considerably slower timescales than neurons within the hindbrain (Figures 4B and S4A). This might indicate a role of forebrain areas in longer timescale integration of stimuli, potentially related to the setting of behavioral states rather than generation of short-timescale behavior.

To describe the amount of information region-specific activity carries about the behavior, we analyzed mutual information between activity in each region and the flick and swim behavior rates. Mutual information between all activity in a given region and the observed motor output reflected the results of the linear model (Figure 4C). While there was a modest increase in mutual information between considering only the sensory stimulus or activity in the trigeminal ganglion, activity in Rh 5/6 of the hindbrain contained as much information about behavior as activity in any other region except for the motor cells themselves (Figure 4C). To further analyze the distribution of information, we combined heat-modulated activity across all regions. Performing principal component analysis revealed that the first five components capture more than 95% of the total variance in heat-modulated activity (Figures S4F and S4G). Together, these components had mutual information of 3.8 bits with the motor output, an increase of only 4% over Rh 5/6 alone. Therefore, our preferred model is that other brain areas—like the pallium, subpallium, or cerebellum—are not directly involved in the described behavior but rather monitor the information for higher-order purposes. Mutual information of motor cells with the motor output is smaller than the entropy

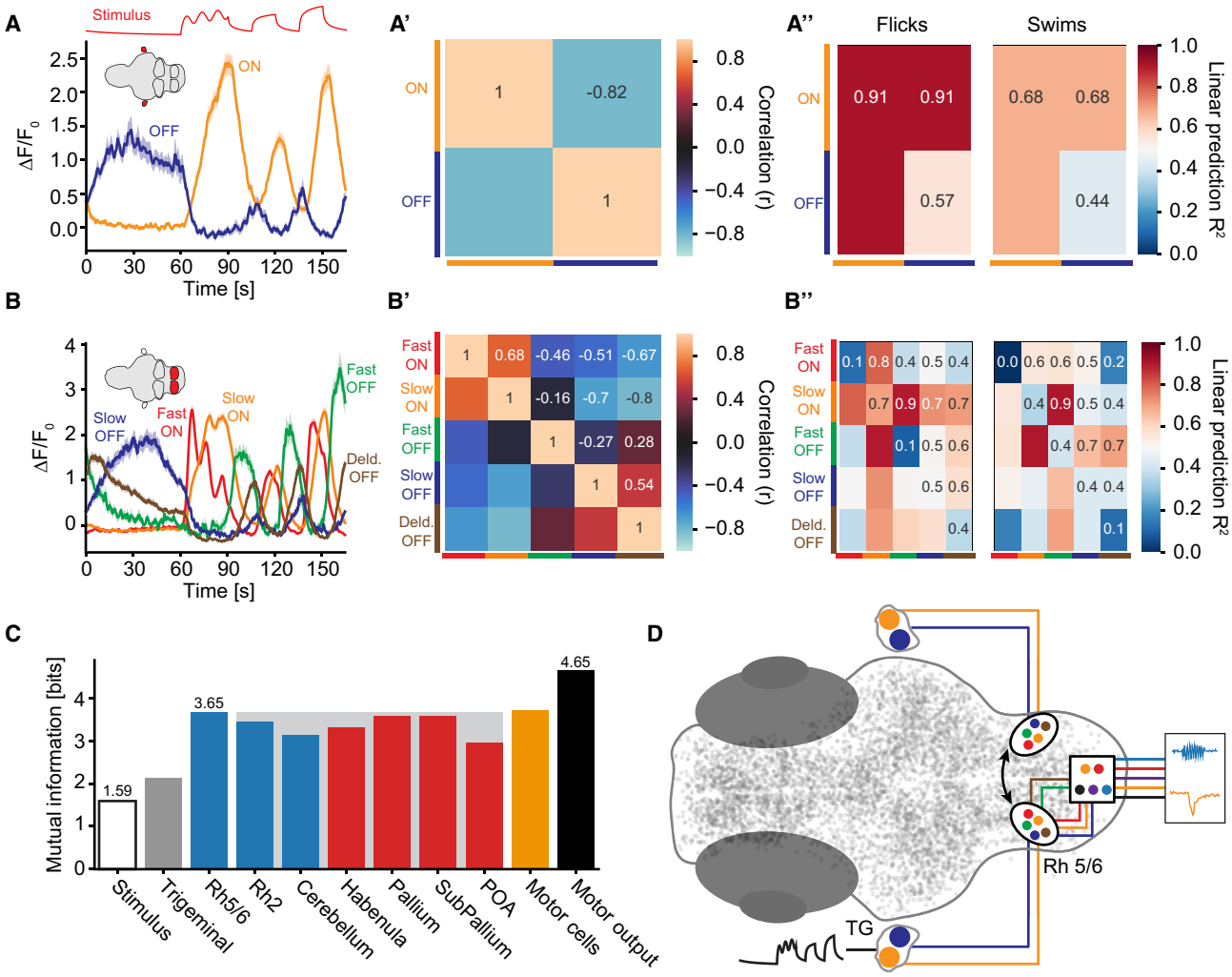

Figure 4. Diversity of Heat Responses Increases in the Hindbrain

(A–A'') Characterization of heat responses in the trigeminal ganglion.

(A) Response types extracted via spectral clustering; ON cells orange (N = 98 cells), OFF cells blue (N = 73 cells), across 10 fish. Thick lines indicate cell-average activity; shading indicates bootstrap standard error.

(A') Pairwise correlations of the response types to quantify similarity.

(A'') Coefficient of determination (R^2) for using one (diagonal) or up to two of the response types to predict flicks (left) or swims (right).

(B–B'') Characterization of heat responses in the Rhombomere 5/6 region of the hindbrain.

(B) Response types extracted via spectral clustering. Fast-ON cells, red (N = 259 cells); slow-ON cells, orange (N = 265 cells); fast-OFF cells, green (N = 24 cells); slow-OFF cells, blue (N = 55 cells); and delayed-OFF cells, brown (N = 92 cells), across 16 fish. Thick lines indicate cell-average activity; shading indicates bootstrap standard error.

(B') Pairwise correlations of the response types to quantify similarity.

(B'') Coefficient of determination (R^2) for using one (diagonal) or up to two of the response types to predict flicks (left) or swims (right). A linear model combining just two activity types was chosen for direct comparison with the trigeminal activity types.

(C) Mutual information with the motor output by knowing the stimulus (hollow bar) or all heat-related activity in the given brain regions (gray trigeminal ganglion, blue hindbrain, red forebrain) or motor cell activity (orange bar). The filled black bar quantifies the entropy in the motor output itself. The height of the gray box indicates mutual information in Rh 5/6 and marks regions not included in the circuit model.

(D) Schematic of response diversification between detection in the trigeminal and cells in Rh 5/6 of the hindbrain, followed by activation of motor cells and finally the generation of motor output (example bout traces on right). Colors indicate response types. The black arrow connecting both hemispheres in Rh 5/6 indicates flow of information suggested by the unilateral trigeminal ablations.

See also Figure S4.

of the behavior itself (Figure 4C), a likely consequence of recording behavior in each imaging plane while not all planes contained motor cells. Shuffling the activity data reduces the number of cells identified through clustering to less than 3% in each region (Figure S4H), arguing that the recovered cell types are a true feature of stimulus representation.

In summary, the data indicate that activity transformation in a trigeminal target area (Figure 4D) is an important step in the observed sensori-motor transformations: this transformation is necessary to explain the behavioral output, while later stimulus transformations do not seem to increase information about the motor output (Figure 4C).

A Dynamic Circuit Model Captures Activity Transformations and Generation of Behavior

To better understand and quantify the sensori-motor transformations underlying heat-evoked swimming behavior, we sought to build a dynamic circuit model that is constrained by the behavior and the observed neuronal activity. This model describes four independent, sequential transformations: first, sensory stimulus to activity in the trigeminal; second, activity in the trigeminal to activity in Rh 5/6; third, the transformation from Rh 5/6 to motor cells; and fourth, the generation of behavior given the activity in the motor cells (Figure 5). Since motor cell firing and timing of individual swim bouts was highly variable (Figures S1H and S1I), our model predicts rates of motor cell firing and behavior, respectively, rather than individual events.

The transformation from sensory stimulus to trigeminal activity is a dynamic process relying on temporal processing. We therefore fit a model that combines linear multiplication of the sensory input with convolution by a temporal filter (Figure 5A). Both the multiplicative term and filter parameters were fit using Markov-chain-Monte-Carlo sampling, obtaining confidence intervals on the parameters in the process (Hastings, 1970; see STAR Methods). Since stimulus encoding relied on a non-linear transformation, a cubic non-linearity accounted for differences in mapping between stimulus strength and neuronal activity (Figure S5A and S5B). This approach allowed explaining the observed ON- and OFF-type activity in the trigeminal ganglion in terms of the sensory stimulus, as evidenced by the close juxtaposition of the fits and true activity (Figures 5A1 and 5A2). As expected, the linear factors of the model demonstrate an activation of the ON type and an inhibition of the OFF type by the sensory stimulus. And at this stage, a linear filter resembling a nuclear calcium indicator kernel (Kawashima et al., 2016) is sufficient to capture the transformation from stimulus to activity (Figures 5A1 and A2).

Our previous analysis indicated that the most important transformation occurs in Rh 5/6 of the hindbrain. To explain the response types in this region in terms of trigeminal neuron activity, we employed the same approach: a linear combination of trigeminal activity followed by convolution with a filter and an output nonlinearity (Figures 5B and S5C–S5G). Two cell types in this hindbrain region, slow-ON and slow-OFF, were similar to the trigeminal cell types. The slow-ON type has slightly faster dynamics than the trigeminal ON cells, as evidenced by the adaptive component in its filter, and it is almost exclusively driven by excitatory inputs from the trigeminal ON cells (Figure 5B1). We note that, since adaptive filters compute a derivative of their input, they are prone to increase noise. The long timescales observed in the filters could therefore reflect a mixture of suppressing noise in the best fit (see Figure S5H for a simulation) as well as true neuronal processes underlying adaptation and bursting (Bean, 2007). The slow-OFF type is an almost direct copy of trigeminal activity, as evidenced by a filter that is essentially a delta function (Figure 5B2). The three other cell types in Rh 5/6 critically relied on inhibitory inputs (Figures 5B3–5B5). While trigeminal neurons express a variety of neurotransmitters, they are largely glutamatergic (Lazarov, 2002). Imaging activity in Rh 5/6 in the presence of transgenic glutamatergic and gabaergic labels revealed that both the slow-ON and slow-OFF cell types consist of both excitatory and inhibitory neurons (Figure S5I). We therefore used the slow-ON and slow-OFF types in the model to provide the required inhibition instead of the trigeminal inputs. Both the newly arising fast-ON and fast-OFF types required inhibition by slow-OFF cells, albeit to differing degrees. Furthermore, as suggested from their activity profiles, both their filters signal strong adaptation (Figures 5B3 and 5B4). The last activity type, termed a ‘‘delayed-OFF’’ type, as it had fast kinetics but started to respond after the fast-OFF cells, relied on inhibition by the slow-ON type. The linear filter of this type potentially hints at a mixture of integration and differentiation, which would also be suggested by the activity profile itself (Figure 5B5). To test the importance of temporal filtering and hence the dynamic structure of our model, we fit an alternative model in which no linear filters were applied for cell types in Rh 5/6. As expected, such a model still explains the activity of slow-ON and -OFF types well, whereas the activity of the fast-ON and -OFF types could not be recreated from trigeminal inputs without filtering (Figure S5J). This indicates that temporal filtering of activity is a critical step in creating important response types observed in Rh 5/6.

Since motor cells in the brain did not track the stimulus itself but, much like the behavior, had a probabilistic chance of firing depending on stimulus strength, we used a simple linear rate-coding model for the transformation from heat-modulated hindbrain activity to activity rates in the motor cells (Figure 5C). Namely, linear combinations of activity in Rh 5/6 cell types explained the activity of each identified motor cell type (Figure 3). Notably, all heat-modulated cell types in Rh 5/6 contribute to the activity of one or multiple motor cell types with varying combinations of activating and inhibiting influences. This is consistent with the mix of excitatory and inhibitory neurons revealed for each cell type in this region (Figures 5C1–5C5 and S5I). Most motor cell types are activated by the slow-ON type, with the expected exception of spontaneous-motor cells, which receive strong excitation from slow-OFF cells almost exclusively (Figure 5C5). This paradoxical control of spontaneous behavior by a stimulus-driven cell type is necessary to explain their lack of activity during stimulation. Interestingly, ‘‘swim’’ cells receive their strongest excitation from the fast-OFF cell type (Figure 5C3), consistent with the requirement of this cell type in explaining swimming behavior via a simple linear model (Figure 4B’’).

The last stage of the model linearly links motor cell output to the observed swim and flick behavior (Figure 5D). Both of these behaviors are strongly activated by the all-motor and evoked-motor cells. Flick cells, overall, have a weak contribution to both behaviors; however, as expected, while they inhibit swims, they activate flicks. Swim cells, on the other hand, have a strong contribution to swims, but do not influence flicks (Figure 5D).

In summary, we could derive a realistic dynamic circuit model that can explain the observed transformations in activity from

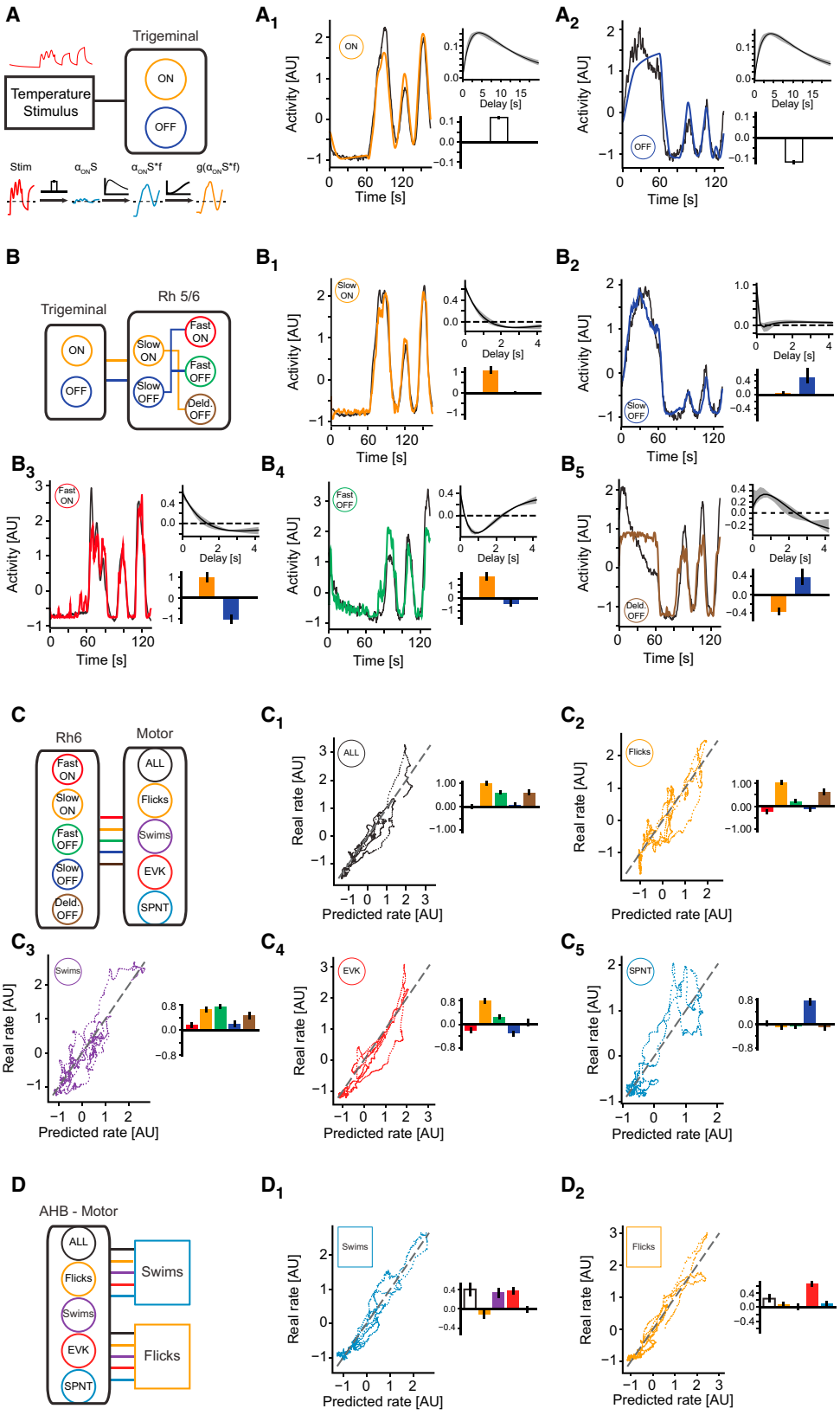

(legend on next page)

sensation to behavioral output and that makes clear and testable predictions about the underlying circuit.

The Circuit Model Can Predict Behavior and Neuronal Responses to Novel Stimuli

In the dynamic circuit model of the sensori-motor transformations (Figure 6A), each stage of the model was fit independently. Hence, errors could accumulate across the model, preventing prediction of behavioral output in response to sensory input. Therefore, as a first test of the model, we tried to predict the behavioral output of the experiments that were used to fit the model given the sensory input. Both the rates of swims and flicks were very well predicted by the circuit model (Figure 6B), indicating that errors do not accumulate across the different stages.

To test the generality of the model, we evaluated its prediction in response to a sensory stimulus not used for fitting. To this end, we used a heat stimulus with distinct temporal dynamics consisting of three temperature steps and a ramp followed by a faster oscillating sine wave (Figures 6A and S6A). This stimulus served as a test input to our circuit model to compare the prediction of flick and swim behavior to the actual behavioral rates produced by fish during those experiments. The model did very well in predicting behavior to this novel stimulus, explaining close to 90% of the variance in both flick and swim behaviors (Figure 6C). This indicates that the model does generalize across stimuli of different dynamics.

Encouraged by these results, we wondered if it might be possible to identify the different heat-response types present in Rh 5/6 in this experimental set using model predictions as regressors. Probing activity using the model predictions indeed recovered cells with correlated activity for each predictor (Figure S6B). Clustering cells by correlation into types recovered type-average activity that matched the individual model predictions to a large extent, as evidenced by the close juxtaposition of predicted and cluster average activity (Figure 6D). Importantly, the average activity profiles of the types matched expectations. This can be seen by comparing average activity of fast-ON with slow-ON types. Here, as in the other experiment, fast-ON cells showed quicker onset responses followed by adaptation compared to a more sustained profile in the slow type (Figure 6D). The test stimulus set also uncovered that fast-OFF cells not only increase their activity on temperature decline but seem to be especially inhibited during temperature rises. This is revealed by an increase in activity in this cell type before offset of the sine stimulus but concomitant with a decrease in Fast-ON activity (around 100 s into the trial instead of 115 s) (Figure 6D). Additionally, we compared the relative abundance of cell types recovered by the model prediction with the abundance of the same cell types in the original experiments. This analysis revealed a good agreement in relative abundance of cell types (Figure S6E), suggesting that the model prediction indeed recovered the same set of hindbrain cells that were originally identified (Figure 4B).

Interestingly, the prediction of swims and flicks depends to a different extent on accurate representation of Rh 5/6 activity. Using the model without temporal filtering (Figure S5J), prediction of flicks is nearly as good as for the full model, while the prediction of swims is considerably worse for both stimuli, as evidenced by a clear drop in explained variance (Figures S6C and S6D). This is in line with the ability to predict flicks purely based on trigeminal activity (Figure 4A''). As expected, this comparison model performs much worse in identifying fast-ON and fast-OFF cells in Rh 5/6 in response to the test stimulus than the full model (Figure S6F).

In summary, we could demonstrate that our activity-constrained circuit model generalizes to novel stimuli and is able to predict both behavioral output and intermediate neuronal activity in this context. This argues that the model accurately represents computations during sensori-motor transformations in heat perception.

Figure 5. A Dynamic Model of Sensori-motor Transformation during Heat Perception

(A) Schematic of the first model stage relating sensory heat input to activity in the two trigeminal cell types. Red curve depicts sensory stimulus of experiments used for fitting the model. Bottom is a schematic depiction of the influences of the individual components (linear factors, filter, nonlinearity) of the dynamic model using the trigeminal ON cell type as an example.

(A1) Model prediction of trigeminal ON activity (orange) and measured activity (black) (left), impulse response of the model filter (top right), and linear coefficient (bottom right).

(A2) Model prediction of trigeminal OFF activity (blue) and measured activity (black) (left), impulse response of the model filter (top right), and linear coefficient (bottom right).

(B) Schematic of the second model stage, which relates trigeminal output activity to the activity types observed in Rh 5/6 of the hindbrain. Note that the three types in the right column rely on indirect inhibition via the slow ON or slow OFF types.

(B1) Model prediction of slow-ON activity (orange) and measured activity (black) (left), impulse response of the model filter (top right) and the linear coefficients for the trigeminal ON (orange) and OFF (blue) cells (bottom right).

(B2–B5) Same as (B1), but for slow-OFF (B2), fast-ON (B3), fast-OFF (B4), and delayed-OFF (B5) types.

(C) Schematic of the third model stage relating output rates in the hindbrain units to activation rates of the motor-correlated cells.

(C1) Scatterplots of actual versus predicted output rates of modeled all-motor activity (left) and the linear coefficients for the fast-ON (red), slow-ON (orange), fast-OFF (green), slow-OFF (blue), and delayed-OFF (brown) types.

(C2–C5) Same as (C1), but for flicks (C2), swims (C3), evoked-motor (C4) and spontaneous-motor (C5) types.

(D) Schematic of the last model stage relating output rates of the motor correlated cells to behavioral rates.

(D1) Scatterplots of actual versus predicted behavior rates of modeled swim output (left) and the linear coefficients for the all-motor (black), flick (orange), swims (purple), evoked-motor (red) and spontaneous-motor (blue) cells.

(D2) Same as (D1), but for predicted behavior rates of flick output.

Shading and error bars indicate 99% confidence intervals after sampling from the posterior distribution.

See also Figure S5.

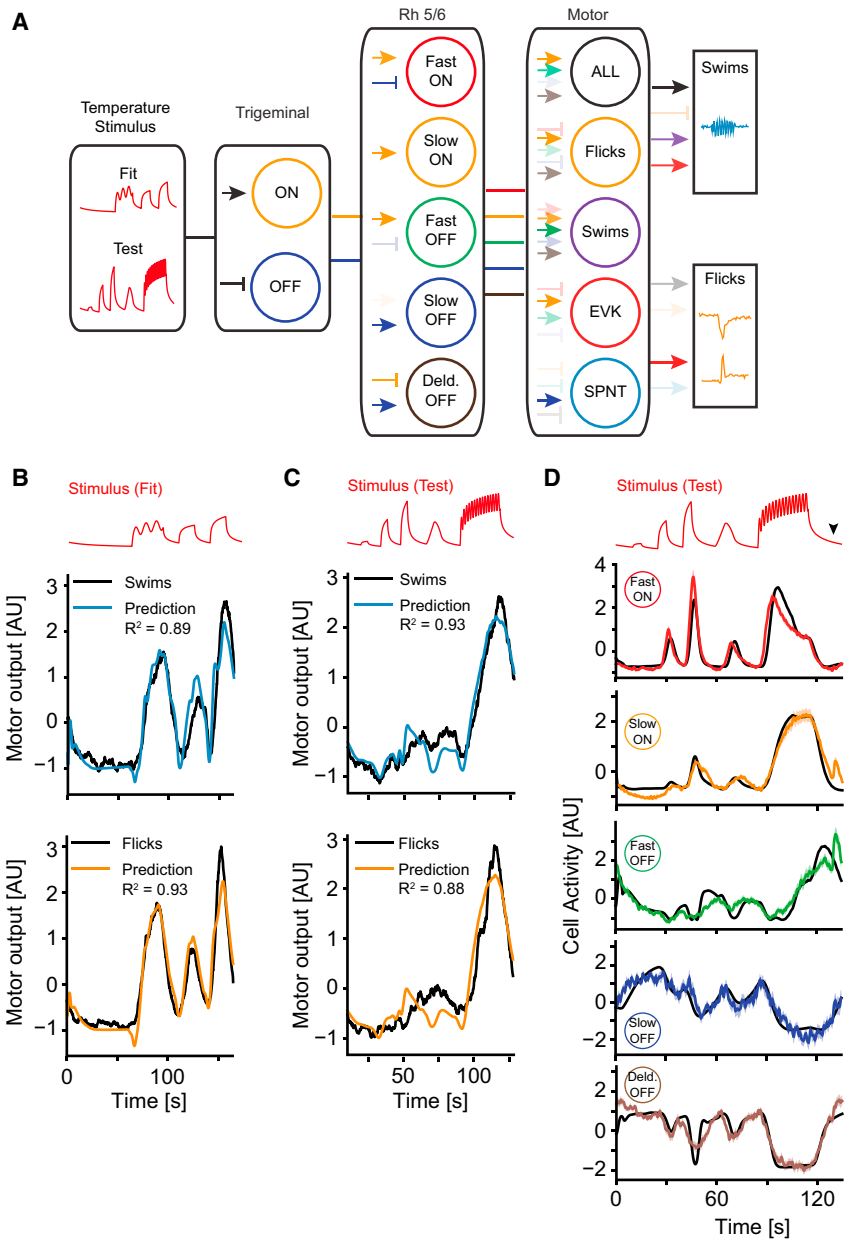

Figure 6. The Model Predicts Behavioral and Neural Activity in Response to Novel Stimuli

(A) Schematic of the full feedforward model. Colored arrows depict the mixing of sensory input or activity in a previous stage, with arrowheads indicating excitatory and bars indicating inhibitory effects. Opacity of arrows indicates the weight of a given component in the fit.

(B) Prediction of swims (top) and flicks (bottom) based on the model for the same experiments that were used to fit the model. Colored lines represent prediction; black line is observed behavior convolved with the calcium kernel. Stimulus depicted on top for reference.

(C) Prediction of swims (top) and flicks (bottom) based on the sensory input delivered and motor output observed during the heat and tap experiments. Note that periods in which the behavior is affected by the tap itself have been excluded from the plot. Colored lines represent prediction; black line is observed behavior convolved with the calcium kernel. Stimulus depicted on top for reference.

(D) Cluster average activity (colored lines) of the indicated types versus each model predicted regressor (black line). Stimulus is depicted on top for reference. The black arrowhead indicates timing of the tap which was present in this test stimulus, but which was not included in our modeling. Shading indicates bootstrap standard error (N = 14 to 156 cells, across 12 fish).

See also Figure S6.

DISCUSSION

The sense of temperature is conserved from mammals (Murakami and Kinoshita, 1977) to bacteria (Maeda et al., 1976), but how information about environmental temperature is represented across the brain, especially in vertebrates, is largely unknown. In this study, we combined a novel experimental paradigm with theoretical modeling approaches to delineate the circuits and computations that underlie the transformation from temperature sensation to behavior.

A Brain-wide Atlas of Temperature-Modulated Activity

Previous work across animal species has provided important insight into the cellular and molecular mechanisms and circuit logic of temperature detection; however, brain-wide analysis of temperature-modulated activity is lacking. Here, we mapped neurons with heat-modulated activity across a whole vertebrate brain and found that the representation of temperature is widespread and especially prominent in the forebrain and hindbrain. As expected, the trigeminal ganglion, a somatosensory area, contains heat-sensitive neurons. However, only a small fraction of cells in the trigeminal ganglion responded to our heat stimuli (Figure 2E), which were well outside the noxious range (Figure 1B). This is in line with previous reports in mice, in which only few trigeminal neurons detect innocuous warmth, while many respond to noxious heat (Yarmolinsky et al., 2016). The rhombomere 5/6 region, which receives trigeminal projections (Pan et al., 2012), contained prominent clusters of heat-modulated cells. Furthermore, responsive cells were aggregated in the dorsal cerebellum, in both habenulae, and in pallium and sub-pallium. This likely indicates that temperature not only influences behavior directly but also provides meaningful information for higher-order processes controlled by the brain. Heat-modulated activity in the pre-optic area hints at a potential functional conservation of this structure, which is involved in the regulation of body temperature in mammals (Boulant, 2000) and behavioral fever in toads (Bicego and Branco, 2002).

Functional Diversity of Temperature Encoding

Across the brain, we find that temperature is encoded by both ON- and OFF-type cells. A separation of temperature coding into ON and OFF cells also emerged as a common principle from previous studies in flies (Frank et al., 2015; Liu et al., 2015) and mice (Ran et al., 2016). Such a separation of sensory coding into ON and OFF channels has been thought to aid in coding efficiency (Gjorgjieva et al., 2014) and may serve to mitigate effects of correlated noise. Comparing heat-responsive cell types across regions revealed clear differences in response dynamics. Sensory neurons in the trigeminal fall into two strongly anti-correlated ON and OFF types with sustained responses. In the hindbrain, on the other hand, more divergent response types could be identified, including cells that showed strong adaptation and are therefore most sensitive to temperature changes. While we observe a combination of sustained and transient ON and OFF cells in Rh 5/6 (Figure 4B), second-order neurons in the mouse spinal cord represent warming exclusively with sustained responses and cooling in a transient manner (Ran et al., 2016). We haven't explicitly presented cold stimuli in this study, and it will be interesting to reveal whether our ON and OFF cells simply reverse their behavior in response to cold stimuli or if these are encoded by a different circuit altogether.

We believe that the other heat-encoding brain regions, like the pallium and pre-optic area, serve primarily to monitor heat stimuli for higher-order purposes and do not directly contribute to the sensori-motor transformation. For example, cell types harbored in these regions seem to represent temperature on distinctly slower timescales (Figures S4B–S4E), which could indicate that these cells set long-term states rather than control behavior itself.

Furthermore, by comparing neuronal responses to temperature stimuli as well as escape-inducing acoustic taps, we could probe the logic of stimulus separation and integration. While both stimulus modalities were clearly separated on the level of the trigeminal ganglia and hindbrain, multimodal responses emerged in forebrain areas (Figure 2F). This might indicate that cell types arise in these higher-order structures, which encode stimulus valence rather than the specific stimulus modality.

Stimulus and Behavior Separate Motor Activity across the Brain

Using correlational analysis, we mapped motor-related activity across the brain. Compared with the stimulus representation, motor-related cells are considerably more localized. A large fraction of motor cells is found in the anterior hindbrain as well as in the cerebellum, slightly ventral of the stimulus-related cell clusters. On the other hand, only a small fraction of cells in the forebrain displayed motor-correlated activity.

A simple criterion based on tail dynamics allowed subdividing the head-embedded behavior into two broad classes, "swims" and "flicks." Swims represent bouts which likely correspond to straight swims and routine turns in freely swimming behavior, while flicks are unilateral tail deflections that likely correspond to strong, in-place turns. Mirroring the difference in behavioral output, we find separate pools of cells that are correlated with swims and flicks, indicating that separate pools of cells are used to initiate these different behaviors at the level of the hindbrain. This is similar to the subdivision of reticulo-spinal neurons for straight swim or turn initiation (Huang et al., 2013). In line with ipsilateral cells controlling directional turns (Orger et al., 2008), cells encoding left flicks are more prominent in the left hemisphere of the hindbrain and vice versa (70% of cells are ipsilateral, Figure 3F).

We also identified stimulus-specific motor cells. "Evoked-motor" cells are activated almost exclusively during bouts in which the stimulus laser is on, while "spontaneous-motor" cells are mostly active during spontaneous bouts in the absence of our heat stimulus (Figure S3B). This separation might underlie temperature-induced changes in bout structure such as observed increases in average bout speed caused by temperature increases in freely swimming larval zebrafish (Haesemeyer et al., 2015). That spontaneous and evoked behaviors are controlled by separate pools of cells is in contrast to *Aplysia*, where changes in distributed activity in the same pool of cells account for differences in spontaneous and evoked behaviors (Wu et al., 1994). Previous studies in zebrafish, however, support a coding strategy whereby different behavioral modules are controlled by separate pools of cells (Orger et al., 2008; Thiele et al., 2014).

A Dynamic Circuit Model of Sensori-motor Transformations during Heat Perception

Models constrained by behavioral and physiological data provide important insight into the logic of sensori-motor transformations (Clark et al., 2013). Recently, modeling has been used in the larval zebrafish to understand processes underlying prey selection (Bianco and Engert, 2015) as well as the generation of the optomotor response (Naumann et al., 2016). This approach resulted in a realistic circuit model of optomotor-induced turning, revealing the circuit logic of binocular stimulus integration (Naumann et al., 2016). We similarly used known anatomy and observed neural activity to derive a realistic circuit model of temperature perception. Correlational analysis strongly suggested that a critical step in the sensori-motor transformations is the observed change of temperature representation between the trigeminal ganglia neurons and their Rh 5/6 target region in the hindbrain. This transformation especially improves the prediction of undulating swim behavior while flicks are already fully predicted at the level of sensory activity in the trigeminal ganglia. Unilateral trigeminal ablations significantly reduced the number of temperature-responsive cells in Rh 5/6 (Figure 2G), and we therefore reasoned that the simplest plausible circuit would consist of the trigeminal neurons, the cells in their Rh 5/6 target area, and the identified motor cells.

Since the stimulus space is characterized by the dynamics of temperature change, we had to extend previous modeling approaches and devise a circuit model that takes these dynamics into account. In fact, a comparison model using static-rate coding alone fails to replicate activity and behavior (Figures S5J, S6C–S6D, and S6F). For stimulus encoding and the transformation of temperature representation in the brain, the model therefore consists not only of linear coefficients but also of filter kernels that are fit for each cell type separately. These filter kernels allow quantification of the dynamical changes in heat representation (Figures 5A and 5B). Using this approach, we find that while slow-OFF cells in Rh5/6 largely copy their trigeminal input,

other cell types, such as the fast-ON and fast-OFF cells, rely on adaptation to transform their inputs.

In the model, the filter kernels are a property of a given cell type, effectively acting as input filters. This is a plausible explanation, as different cell intrinsic processes can lead to the observed spiking adaptation in the fast-ON or -OFF cell type or to more complex interactions between adaptation and bursting behavior, as suggested in the filter of the delayed-OFF type (Blair and Bean, 2003; Friedman et al., 1992; Kernell and Monster, 1982; Pedarzani and Storm, 1993). Further experiments using patch-clamp recording in identified cells are needed to decide whether these are indeed properties of the cells or rather emerging features of local circuits. Furthermore, the model suggests long timescales on the filter properties. These timescales are plausible for processes such as late adaptation observed in motoneurons or hippocampal neurons (Kernell and Monster, 1982; Pedarzani and Storm, 1993) or slow afterpotentials involved in cortical bursting (Bean, 2007; Friedman et al., 1992). On the other hand, the nature of calcium imaging together with the inherent noise precludes a full quantitative interpretation of the filter-kernel timescales (Figure S5H). They do, however, make clear qualitative statements about expected cellular properties, which can be confirmed with future experiments using electrophysiology or voltage imaging.

The Circuit Model as a Framework for Hypothesis Testing

Our circuit model makes clear and testable predictions about the computations and architecture underlying the sensori-motor transformations during heat perception.

While trigeminal fibers are largely glutamatergic (Lazarov, 2002), three of the five cell types identified in Rh 5/6 in the hindbrain rely on inhibitory inputs. The model therefore posits that part of the slow-ON and slow-OFF cell types should be inhibitory interneurons. At the same time, excitatory projections from these neurons onto motor cells are required to explain the activity rates of some motor types. This possibility is well supported by our own experimental results revealing a mix of excitatory and inhibitory neurons for all cell classes in the hindbrain (Figure S5I).

Our previous behavioral study predicted that straight swims should be activated by a strong OFF signal, which is less influential for turning (Haesemeyer et al., 2015). This study supports this conclusion: the circuit model predicts that swim motor cells are most strongly driven by the fast-OFF cell type (Figure 5C3), and in our head-embedded preparation, swims persist after stimulus offset while flicks—likely corresponding to stationary turns—subside quickly (Figure 1F).

The core transformation from the trigeminal to the hindbrain to the motor output is well captured by our dynamic circuit model, which is constrained by a variety of activity measurements and which we validated by testing its predictive power against novel sensory stimuli. Such a brain-wide realistic model that captures the dynamic aspects of sensorimotor transformations is novel in the context of temperature processing and provides a computational and experimental framework for generating testable circuit models of temporal coding. Furthermore, the general model architecture presented here will allow inclusion of modules responsible for higher-order processing, such as observed activity in the cerebellum and forebrain areas, in the future, and it can be easily applied to other stimuli and organisms to capture similar transformations in representation.

STAR★METHODS

Detailed methods are provided in the online version of this paper and include the following:

- KEY RESOURCES TABLE
- CONTACT FOR REAGENT AND RESOURCE SHARING
- EXPERIMENTAL MODEL AND SUBJECT DETAILS
- METHOD DETAILS
  - Imaging and behavior
  - Stimulus characterization
  - Image stabilization
  - Image segmentation
  - Registration and annotation
  - Swim-bout identification and classification
  - Clustering of heat- and motor-related activity
  - Identification of heat- and tap-responsive cells
  - Nearest neighbor distance metrics
  - Information metrics
  - Determination of neurotransmitter types
  - Trigeminal ablations
  - Circuit model
- QUANTIFICATION AND STATISTICAL ANALYSIS
  - Data shuffles
- DATA AND SOFTWARE AVAILABILITY

SUPPLEMENTAL INFORMATION

Supplemental Information includes six figures and can be found with this article online at https://doi.org/10.1016/j.neuron.2018.04.013.

ACKNOWLEDGMENTS

M.H. was supported in part of this project by an EMBO Long Term Postdoctoral fellowship (ALTF 1056-10) and a postdoctoral fellowship by the Jane Coffin Childs Fund for Biomedical Research (61-1468). Research was funded by NIH grants DP1-NS082121, U01NS090449, U19NS104653, and 5R24NS086601 to F.E. and 1DP1HD094764 to A.F.S. We thank Iris Odstrcil for being the ablation consultant on this project. We thank Ruben Portugues, Andrew D. Bolton, James Fitzgerald, and Aravi Samuel for critical discussion and helpful comments on the manuscript.

AUTHOR CONTRIBUTIONS

M.H. conceived the project in discussion with F.E. and A.F.S. and carried out all experiments. D.N.R. and J.M.L. built the 2-photon microscope and IR stimulus delivery and wrote the imaging software. M.H. wrote the online stabilization pipeline and all analysis software, analyzed the data, and built the model. M.H., A.F.S., and F.E interpreted the data and wrote the manuscript.

DECLARATION OF INTERESTS

The authors declare no competing interests.

Received: August 28, 2017
Revised: March 1, 2018
Accepted: April 10, 2018
Published: May 3, 2018

REFERENCES

Bean, B.P. (2007). The action potential in mammalian central neurons. Nat. Rev. Neurosci. *8*, 451–465.

Bianco, I.H., and Engert, F. (2015). Visuomotor transformations underlying hunting behavior in zebrafish. Curr. Biol. *25*, 831–846.

Bicego, K.C., and Branco, L.G.S. (2002). Discrete electrolytic lesion of the preoptic area prevents LPS-induced behavioral fever in toads. J. Exp. Biol. *205*, 3513–3518.

Blair, N.T., and Bean, B.P. (2003). Role of tetrodotoxin-resistant Na+ current slow inactivation in adaptation of action potential firing in small-diameter dorsal root ganglion neurons. J. Neurosci. *23*, 10338–10350.

Boulant, J.A. (2000). Role of the preoptic-anterior hypothalamus in thermoregulation and fever. Clin. Infect. Dis. *31* (*Suppl 5*), S157–S161.

Budick, S.A., and O'Malley, D.M. (2000). Locomotor repertoire of the larval zebrafish: swimming, turning and prey capture. J. Exp. Biol. *203*, 2565–2579.

Cabanac, M., Hammel, T., and Hardy, J.D. (1967). Tiliqua scincoides: temperature-sensitive units in lizard brain. Science *158*, 1050–1051.

Carpenter, A.E., Jones, T.R., Lamprecht, M.R., Clarke, C., Kang, I.H., Friman, O., Guertin, D.A., Chang, J.H., Lindquist, R.A., Moffat, J., et al. (2006). CellProfiler: image analysis software for identifying and quantifying cell phenotypes. Genome Biol. *7*, R100.

Caterina, M.J., Schumacher, M.A., Tominaga, M., Rosen, T.A., Levine, J.D., and Julius, D. (1997). The capsaicin receptor: a heat-activated ion channel in the pain pathway. Nature *389*, 816–824.

Clark, D.A., Biron, D., Sengupta, P., and Samuel, A.D.T. (2006). The AFD sensory neurons encode multiple functions underlying thermotactic behavior in Caenorhabditis elegans. J. Neurosci. *26*, 7444–7451.

Clark, D.A., Gabel, C.V., Gabel, H., and Samuel, A.D.T. (2007). Temporal activity patterns in thermosensory neurons of freely moving Caenorhabditis elegans encode spatial thermal gradients. J. Neurosci. *27*, 6083–6090.

Clark, D.A., Freifeld, L., and Clandinin, T.R. (2013). Mapping and cracking sensorimotor circuits in genetic model organisms. Neuron *78*, 583–595.

Dean, J.B., and Boulant, J.A. (1989). In vitro localization of thermosensitive neurons in the rat diencephalon. Am. J. Physiol. *257*, R57–R64.

Dunn, T.W., Mu, Y., Narayan, S., Randlett, O., Naumann, E.A., Yang, C.-T., Schier, A.F., Freeman, J., Engert, F., and Ahrens, M.B. (2016). Brain-wide mapping of neural activity controlling zebrafish exploratory locomotion. eLife *5*, e12741.

Erzurumlu, R.S., Chen, Z.-F., and Jacquin, M.F. (2006). Molecular determinants of the face map development in the trigeminal brainstem. Anat. Rec. A Discov. Mol. Cell. Evol. Biol. *288*, 121–134.

Frank, D.D., Jouandet, G.C., Kearney, P.J., Macpherson, L.J., and Gallio, M. (2015). Temperature representation in the Drosophila brain. Nature *519*, 358–361.

Freeman, J., Vladimirov, N., Kawashima, T., Mu, Y., Sofroniew, N.J., Bennett, D.V., Rosen, J., Yang, C.-T., Looger, L.L., and Ahrens, M.B. (2014). Mapping brain activity at scale with cluster computing. Nat. Methods *11*, 941–950.

Friedman, A., Arens, J., Heinemann, U., and Gutnick, M.J. (1992). Slow depolarizing afterpotentials in neocortical neurons are sodium and calcium dependent. Neurosci. Lett. *135*, 13–17.

Gallio, M., Ofstad, T.A., Macpherson, L.J., Wang, J.W., and Zuker, C.S. (2011). The coding of temperature in the Drosophila brain. Cell *144*, 614–624.

Gjorgjieva, J., Sompolinsky, H., and Meister, M. (2014). Benefits of pathway splitting in sensory coding. J. Neurosci. *34*, 12127–12144.

Haesemeyer, M., Robson, D.N., Li, J.M., Schier, A.F., and Engert, F. (2015). The structure and timescales of heat perception in larval zebrafish. Cell Syst. *1*, 338–348.

Hastings, W.K. (1970). Monte Carlo sampling methods using Markov chains and their applications. Biometrika *57*, 97–109.

Hedgecock, E.M., and Russell, R.L. (1975). Normal and mutant thermotaxis in the nematode Caenorhabditis elegans. Proc. Natl. Acad. Sci. USA *72*, 4061–4065.

Hoffman, M.D., and Gelman, A. (2014). The No-U-turn sampler: adaptively setting path lengths in Hamiltonian Monte Carlo. J. Mach. Learn. Res. *15*, 1593–1623.

Huang, K.-H., Ahrens, M.B., Dunn, T.W., and Engert, F. (2013). Spinal projection neurons control turning behaviors in zebrafish. Curr. Biol. *23*, 1566–1573.

Julius, D., and Basbaum, A.I. (2001). Molecular mechanisms of nociception. Nature *413*, 203–210.

Kawashima, T., Zwart, M.F., Yang, C.-T., Mensh, B.D., and Ahrens, M.B. (2016). The Serotonergic System Tracks the Outcomes of Actions to Mediate Short-Term Motor Learning. Cell *167*, 933–946.e20.

Kernell, D., and Monster, A.W. (1982). Time course and properties of late adaptation in spinal motoneurones of the cat. Exp. Brain Res. *46*, 191–196.

Kim, D.H., Kim, J., Marques, J.C., Grama, A., Hildebrand, D.G.C., Gu, W., Li, J.M., and Robson, D.N. (2017). Pan-neuronal calcium imaging with cellular resolution in freely swimming zebrafish. Nat. Methods *14*, 1107–1114.

Lacoste, A.M.B., Schoppik, D., Robson, D.N., Haesemeyer, M., Portugues, R., Li, J.M., Randlett, O., Wee, C.L., Engert, F., and Schier, A.F. (2015). A convergent and essential interneuron pathway for Mauthner-cell-mediated escapes. Curr. Biol. *25*, 1526–1534.

Lazarov, N.E. (2002). Comparative analysis of the chemical neuroanatomy of the mammalian trigeminal ganglion and mesencephalic trigeminal nucleus. Prog. Neurobiol. *66*, 19–59.

Liu, W.W., Mazor, O., and Wilson, R.I. (2015). Thermosensory processing in the Drosophila brain. Nature *519*, 353–357.

Madelaine, R., Lovett-Barron, M., Halluin, C., Andalman, A.S., Liang, J., Skariah, G.M., Leung, L.C., Burns, V.M., and Mourrain, P. (2017). The hypothalamic NPVF circuit modulates ventral raphe activity during nociception. Sci. Rep. *7*, 41528.

Maeda, K., Imae, Y., Shioi, J.I., and Oosawa, F. (1976). Effect of temperature on motility and chemotaxis of Escherichia coli. J. Bacteriol. *127*, 1039–1046.

Miri, A., Daie, K., Burdine, R.D., Aksay, E., and Tank, D.W. (2011). Regression-based identification of behavior-encoding neurons during large-scale optical imaging of neural activity at cellular resolution. J. Neurophysiol. *105*, 964–980.

Murakami, H., and Kinoshita, K. (1977). Spontaneous activity and heat avoidance of mice. J. Appl. Physiol. *43*, 573–576.

Naumann, E.A., Fitzgerald, J.E., Dunn, T.W., Rihel, J., Sompolinsky, H., and Engert, F. (2016). From Whole-Brain Data to Functional Circuit Models: The Zebrafish Optomotor Response. Cell *167*, 947–960.e20.

Orger, M.B., Kampff, A.R., Severi, K.E., Bollmann, J.H., and Engert, F. (2008). Control of visually guided behavior by distinct populations of spinal projection neurons. Nat. Neurosci. *11*, 327–333.

Pan, Y.A., Choy, M., Prober, D.A., and Schier, A.F. (2012). Robo2 determines subtype-specific axonal projections of trigeminal sensory neurons. Development *139*, 591–600.

Pedarzani, P., and Storm, J.F. (1993). PKA mediates the effects of monoamine transmitters on the K+ current underlying the slow spike frequency adaptation in hippocampal neurons. Neuron *11*, 1023–1035.

Portugues, R., Feierstein, C.E., Engert, F., and Orger, M.B. (2014). Whole-brain activity maps reveal stereotyped, distributed networks for visuomotor behavior. Neuron *81*, 1328–1343.

Portugues, R., Haesemeyer, M., Blum, M.L., and Engert, F. (2015). Whole-field visual motion drives swimming in larval zebrafish via a stochastic process. J. Exp. Biol. *218*, 1433–1443.

Ran, C., Hoon, M.A., and Chen, X. (2016). The coding of cutaneous temperature in the spinal cord. Nat. Neurosci. *19*, 1201–1209.

Randlett, O., Wee, C.L., Naumann, E.A., Nnaemeka, O., Schoppik, D., Fitzgerald, J.E., Portugues, R., Lacoste, A.M.B., Riegler, C., Engert, F., and Schier, A.F. (2015). Whole-brain activity mapping onto a zebrafish brain atlas. Nat. Methods *12*, 1039–1046.

Rohlfing, T., and Maurer, C.R., Jr. (2003). Nonrigid image registration in shared-memory multiprocessor environments with application to brains, breasts, and bees. IEEE Trans. Inf. Technol. Biomed. *7*, 16–25.

Salvatier, J., Wiecki, T.V., and Fonnesbeck, C. (2016). Probabilistic programming in Python using PyMC3. Peer. PeerJ Computer Science *2*, e55.

Satou, C., Kimura, Y., Hirata, H., Suster, M.L., Kawakami, K., and Higashijima, S. (2013). Transgenic tools to characterize neuronal properties of discrete populations of zebrafish neurons. Development *140*, 3927–3931.

Schepers, R.J., and Ringkamp, M. (2010). Thermoreceptors and thermosensitive afferents. Neurosci. Biobehav. Rev. *34*, 177–184.

Severi, K.E., Portugues, R., Marques, J.C., O'Malley, D.M., Orger, M.B., and Engert, F. (2014). Neural control and modulation of swimming speed in the larval zebrafish. Neuron *83*, 692–707.

Thiele, T.R., Donovan, J.C., and Baier, H. (2014). Descending control of swim posture by a midbrain nucleus in zebrafish. Neuron *83*, 679–691.

Wu, J.Y., Cohen, L.B., and Falk, C.X. (1994). Neuronal activity during different behaviors in Aplysia: a distributed organization? Science *263*, 820–823.

Yarmolinsky, D.A., Peng, Y., Pogorzala, L.A., Rutlin, M., Hoon, M.A., and Zuker, C.S. (2016). Coding and Plasticity in the Mammalian Thermosensory System. Neuron *92*, 1079–1092.

Zahl, S. (1977). Jackknifing an index of diversity. Ecology *58*, 907–913.

STAR★METHODS

KEY RESOURCES TABLE

REAGENT or RESOURCE	SOURCE	IDENTIFIER
Experimental Models: Organisms/Strains		
Tg(elavl3:H2B-GCaMP6s)	Freeman et al., 2014	jf5
Tg(elavl3:GCaMP6s)	Kim et al., 2017	a13203
TgBAC(slc17ab:LOXP-mCherry-LOXP-GAL4) – vglut2a;mCherry	Satou et al., 2013	nns21Tg
TgBAC(gad1b:LOXP-RFP-LOXP-GFP) – gad1b:RFP	Satou et al., 2013	nns26Tg
Tg(elavl3:H2B-RFP)	Randlett et al., 2015	NA
Software and Algorithms		
C# (.NET Framework 4.0; Two-photon acquisition)	This study	NA
Python analysis software	This study	NA
FIJI (ImageJ; anatomy)	NIH	http://fiji.sc
Cell profiler (Nuclear segmentation)	Broad Institute	http://cellprofiler.org
RegionSelector – to segment regions in imaging stacks	This study	https://github.com/haesemeyer/RegionSelector

CONTACT FOR REAGENT AND RESOURCE SHARING

Further information and requests for resources and reagents should be directed to and will be fulfilled by the Lead Contact, Florian Engert (florian@mcb.harvard.edu).

EXPERIMENTAL MODEL AND SUBJECT DETAILS

All experiments were conducted on 6-7 days post fertilization zebrafish homozygous for the *nacre* mutation expressing the transgenes indicated below. The sex of the larva is not defined at this early stage. Fish were fed paramecia from day 5 onward. All experiments followed the guidelines of the National Institutes of Health and were approved by the Standing Committee on the Use of Animals in Research of Harvard University.

All experiments used for mapping heat responsive neurons and for model derivation used fish expressing nuclear Elavl3:H2B-GCaMP6s fish (Freeman et al., 2014). Experiments combining heat and taps as well as trigeminal ablations were performed in fish expressing cytoplasmic Elavl3:Gcamp6s (Kim et al., 2017). We note that while the decay time-constants for cytoplasmic and nuclear GCaMP are different, we found this effect to be negligible given the slow timescales of our temperature stimulus.

To develop the scan stabilization protocol Elavl3:H2B-RFP fish expressing RFP in all neuronal nuclei were used (Randlett et al., 2015).

To identify neurotransmitter types of heat modulated neurons, progeny of crosses between Elavl3:H2B-Gcamp6s (Freeman et al., 2014) and either vglut2a:mCherry (Satou et al., 2013) or gad1B:dsRed (Satou et al., 2013) expressing fish were used.

METHOD DETAILS

Since almost all analysis in this study was performed in an automated manner, no blinding or randomization was performed. All sample sized were fixed before the start of experiments and all animals were analyzed except those that freed themselves from the preparation during imaging or that died during the experimental procedure.

Imaging and behavior

Larval zebrafish were embedded in 2.5% medium melt agarose (Fisher scientific, USA) and their tails were freed the night before the experiment. Experiments were conducted in a custom built 2-photon microscope and run using custom written software in C# (Microsoft, USA). Heat stimuli were delivered using a 1W 980nm fiber-coupled diode laser (Roithner, Austria) coupled into a collimator (Aistana Inc., USA) placed under the microscope objective 4 mm in front of and 1.2 mm above the head of the zebrafish larva pointing downward at an angle of 16.5 degrees. The laser power was controlled by the computer via a laser diode driver (Thorlabs, USA). We note that the 980 nm laser itself did not excite GCaMP fluorescence due to the low photon density.

The main mapping experiments consisted of the imaging of 30 individual planes, spaced 2.5 μm apart. In each plane 3 trials of the stimulus depicted in Figure 1B were presented.

The heat and tap experiments consisted of imaging 4 individual planes, spaced 5 μm apart. In each plane 25 trials of the stimulus depicted in Figure S1G were presented.

To avoid excessive heating of the preparation by scanning over the eyes, custom exclusion masks were created for each experiment in which the eyes were in the field of view, restricting the scan-lines such that the eyes were excluded from the field of view.

Imaging was performed at 2.4 Hz - 3 Hz and all imaging data was interpolated to a 5 Hz timebase before further analysis. Tail-tracking data was acquired at 100 Hz. All behavioral features such as identifying and classifying bouts were performed at this timebase, however, for all comparisons of behavior and imaging, the behavioral data was downsampled to a 5 Hz timebase.

Stimulus characterization

To measure the temperature induced in larval zebrafish by the laser stimulus a thermistor with the same dimension and absorption characteristics as larval zebrafish was used (Warner instruments, USA; Haesemeyer et al., 2015). The thermistor was embedded in the same low-melting point agarose as the larval zebrafish and the laser was positioned accordingly (Madelaine et al., 2017). For each stimulus used, temperature changes in the thermistor were subsequently recorded. While tissue absorption is not homogeneous for larval zebrafish, modeling of thermal flux revealed that over the short length scales at this age there won't be an uneven distribution of temperature within the head of larval zebrafish due to the thermal conductivity of water within about 250 ms of stimulus onset. In other words, equilibration happens much faster than the timescales of our stimulus (not shown). Furthermore, the size of the laser spot was set such that it is larger than the head of the fish.

Image stabilization

To counter heat-induced deformations of the preparation, before each plane was scanned a ± 5 μm sized pre-stack consisting of 21 slices spaced 0.4 μm apart was acquired. During scanning, each acquired plane was cross-correlated with each plane in the pre-stack and using a low-pass filter the position of the objective was adjusted online so as to minimize z-drift. Since the heat induced drift observed in Elavl3:H2B-RFP stacks followed very reproducible kinetics these were used to predict the movement induced by heating during our experiments to induce very slight movements in the predicted direction. This served to overcome the delay induced by the low-pass filter.

A second alignment step was performed post-acquisition. Here each individual imaging plane was assigned to the most likely plane in the pre-stack that it corresponds to via correlation. The fluorescence timeseries of each segmented region was subsequently corrected by normalizing it with the resting fluorescence of this region in the pre-stack.

Image segmentation

Cells in each plane were segmented anatomically. To correct for motion artifacts individual planes in each timeseries were re-aligned based on image cross-correlations (Miri et al., 2011). For nuclear GCaMP experiments, individual nuclei were subsequently segmented using Cell Profiler (Carpenter et al., 2006). To resolve merged nuclei in areas of low contrast, objects larger than a typical nuclear size were divided into subregions based on pixel timeseries correlations. For experiments using cytoplasmic GCaMP, custom written software was used to identify individual cells. Each image was processed using a minimum and a maximum filter tuned to nuclear size. Points where the differences between the two filtered results crossed a threshold (at least 20% of the average region brightness) were considered potential cell centroids. After including seed pixels around the centroids individual regions were grown in a greedy manner, incorporating pixels that were better correlated to their own current average activity than to neighboring averages. Resulting correlations masks were intersected with anatomical masks based on cell size to obtain the final segmentation.

Registration and annotation

3D image registration based on CMTK (Rohlfing and Maurer, 2003) was used to create a nuclear GCaMP-6 s reference stack to which all experimental stacks were registered as described elsewhere (Portugues et al., 2014; Randlett et al., 2015).

The reference brain was used to annotate anatomical regions of interest based on Z-Brain annotations (Randlett et al., 2015).

Swim-bout identification and classification

Swim bouts were identified as described previously (Portugues et al., 2015), namely based on the windowed standard deviation of the tail cumulative angle trace crossing a threshold. The mode-centered cumulative angle trace a of each bout was subsequently used to assign the following score:

$$bias = \frac{\sum_a a}{\sum_a |a|}$$

Right flicks were defined as bouts with a bias < -0.8, left flicks as bouts with a bias > 0.8 and all other bouts were defined as "swims." These cutoffs were chosen since the histogram of all bias scores has a minimum at those points.

Clustering of heat- and motor-related activity

To identify motor related activity, motor regressors were created by convolving a bout start trace with an exponential calcium kernel with a decay half time of 3 s. This decay time was derived from motor triggered averages across hindbrain neurons. Behavioral subtype regressors were created by only considering bouts of a given type. The behavioral regressors that differentiate stimulus and rest periods were created by only considering motor events during those respective phases. Every cell with a correlation of at least 0.6 to at least one motor regressor was considered a "motor cell." Since not all behaviors were observed in all imaging planes, cells were only assigned to a more specific category (such as swims versus all bouts) if the correlation to the more specific regressor was significantly higher ($p < 0.01$, bootstrap hypothesis test) than to any more general regressor.

To identify heat responses across the whole brain spectral clustering was performed on a subset of cells since computing a pairwise correlation matrix of all cells and then performing clustering was not feasible. To arrive at a "canonical subset" for clustering the following filtering steps were performed. First for each cell the activity standard deviation during stimulus periods versus the standard deviation during rest periods was computed. All cells for which the standard deviation during stimulation was not greater than the standard deviation during rest were excluded, reasoning that those cells are unlikely to be stimulus modulated. Furthermore, all cells that had a correlation > 0.4 to a motor regressor were removed. This reduced the original number of cells from 699,840 down to 53,728 cells. For all these cells the pairwise correlations were computed. Any cells that did not have at least 20 partners across at least 3 fish that each explained 40% of the cells variance were discarded. The reasoning behind this step was to enrich the considered set for canonical stimulus responses at the expense of discarding any rare response types. After this step 19,389 cells or 2.8% of the original amount remained. We note however, that asking for merely one additional partner is responsible for 80%

of the observed reduction. After arriving at the filtered set of cells the trial-average response of each remaining cell was computed and spectral clustering with pairwise correlations as similarity matrix asking for 6 total clusters was performed. Subsequently the cluster averages were used as regressors, probing the entire set of 699,840 cells. Each cell that had a correlation $\geq$ 0.6 was included in the final cell clusters. Across the resulting clusters about half the cells came from the original "canonical set" while the other half was made up of previously discarded cells.

To identify heat modulated cells in specific brain regions we used the transformations computed during image registration of our experimental stacks together with our manual segmentation to assign each nuclear centroid to a brain region. From each brain region all cells that were correlated > 0.4 to any motor regressor were discarded. Since the number of cells in each region was much smaller than for the whole brain no further filtering was necessary and spectral clustering was performed on all the non-motor correlated cells. Overall the aim was to obtain as many different response types as possible. Setting the number of retrieved clusters to 6, at least one unstructured cluster was obtained in each region. The averages of remaining clusters were subsequently again used as regressors to identify responsive cells in the given region via a correlation $\geq$ 0.6 to the cluster average. Highly correlated clusters ($r > 0.9$) were subsequently merged. This simplified display of the data but had no influence on the further analysis (data not shown) as the highly correlated sister-clusters did not add explanatory power.

To calculate ΔF/F0 values for reporting cell fluorescence we used the average across the first baseline period as the resting fluorescence F0.

Identification of heat- and tap-responsive cells

To identify heat responsive, tap responsive or mixed cells in the heat and tap experiments the timeseries of individual cells were categorized in the following manner. First using behavioral regressors all cells with a motor correlation > 0.4 were sorted out. Subsequently the period of sinewave heat stimulation (as this created the largest heat responses overall) as well as the period of the tap was used to calculate an activation score *a* averaged across the 25 trials T:

$$a = \frac{1}{25}\sum_{T}\frac{\left|\overline{F_{pre}} - \overline{F_{stim}}\right|}{\sigma_{pre}}$$

Cells for which $a > 2$ were considered responsive for the given stimulus, cells where $a < 0.75$ were considered unresponsive and cells with intermediate scores were discarded. These criteria defined inclusion in the heat-responsive, tap-responsive or mixed categories. We note that these scores are fairly strict and overall identified fewer cells across Rh5/6 than the regressor based identification used in Figure 6.

Nearest neighbor distance metrics

To compute nearest neighbor distance metrics for all cells the transformations obtained during image registration were used to map the centroids of all segmented nuclei into a common reference frame. For each cell of interest, the average distance to its two nearest neighbors of the same or comparison type was subsequently computed. Since nearest neighbor distances are influenced by the number of cells in each type as well, when comparing distances, the number of cells was down-sampled to the amount present in the smaller sample used for the comparison.

Information metrics

To compute the mutual information scores, the required entropies and joint entropies were computed using a jackknife estimate in order to reduce bias on small sample sizes (Zahl, 1977).

To compute an approximation of the mutual information between all region activity and the motor output principal component analysis was used for dimensionality reduction. This was necessary as memory requirements for computing the mutual information estimates grow exponentially with the number of traces considered. All mean cluster activities from all segmented regions were combined and principal components were extracted. The first five principal components explained > 95% of the total variance. These were subsequently used to compute the mutual information between these components and the motor output.

Determination of neurotransmitter types

To determine the neurotransmitter type of heat responsive cells in Rhombomeres 5/6 nuclear GCaMP6s was imaged using the heat stimulus in the presence of either a red vGlut2a (excitatory neurons) or red Gad1b (inhibitory neurons) label. Cells were subsequently segmented as described above and cell type cluster averages were used to identify cells of each type present in Rhombomere 5/6. Cells were subsequently cross-referenced with the transmitter label and expression ratios (positive / negative) were determined.

Trigeminal ablations

For trigeminal ablations the hindbrain of fish expressing cytoplasmic GCaMP6s was first imaged using the heat stimulus to identify heat responsive neurons. Subsequently individual cells in one trigeminal ganglion were ablated using 25 ms long pulses of high laser power (300 mW at sample at 850 nm), starting ventrally in the trigeminal and moving dorsally. In total around 40 pulses were delivered in each experiment resulting in partial destruction of the trigeminal ganglion. Damage was subsequently assessed by anatomical imaging. 2 fish were discarded right after the anatomical assessment, because no damage to the trigeminal was visible. A further set of 4 fish died before completion of the experiment and were therefore not analyzed. All 5 fish that survived the functional post-experiment were still healthy the following day and were included in the analysis. No fish were discarded after analyzing the functional data.

Circuit model

The circuit model was constructed as a feed-forward model from stimulus to behavioral output. The activation A in each stage (Trigeminal ganglion - Rh5/6 region of the hindbrain - Motor cells - Behavior) was described as a linear combination of the activations in the previous stage, optionally convolved with a linear filter f (Trigeminal and Rh5/6) and passed through an output nonlinearity g (Trigeminal and Rh5/6):

$$A_i = g\left(\left(A_{i-1}\beta^T\right) * f\right)$$

The linear filter f was necessary to explain the transformations between different response dynamics. The linear parts of each model stage (β and f) were fit via Markov-chain Monte Carlo using PyMC3 (Salvatier et al., 2016). Since all our likelihoods were differentiable allowing gradient calculation we used the no-uturn sampler in PyMC3 for sample generation (Hoffman and Gelman, 2014). Cubic output nonlinearities were subsequently fit using least-squares optimization in Python. The time-resolution Δt of all models was set to 0.2 s the same as the time resolution of our interpolated imaging traces.

We note that our model does not operate on raw neuronal or behavior traces, but the inputs and outputs of all stages were z-scored. This is a more conservative approach due to the nonlinear relationship between calcium signals and neuronal activity.

Stimulus encoding in the trigeminal ganglion

To capture the encoding of the heat stimulus in the observed trigeminal calcium activity the filter was parametrized as an exponential on/off filter akin to a calcium kernel.

$$f(\Delta t; \tau_{off},\ \tau_{on}) = e^{-\frac{\Delta t}{\tau_{off}}} - \left(1 - e^{-\frac{\Delta t}{\tau_{on}}}\right) \mid\ -20s < \Delta t \leq 0$$

To simplify computation, convolution in the model was expressed via piecewise multiplications such that the predicted output activity $A(t)$ of the trigeminal ON and OFF cells at each time point t was described in terms of the temperature stimulus T(t) as

$$A(t; \beta,\ f) = \beta \sum_{\Delta t} T(t - \Delta t) f(\Delta t) \mid\ -20s < \Delta t \leq 0$$

The prior parameter distributions used for the MCMC process were as follows:

$$\beta \sim \mathcal{N}(0,\ 2)$$

$$\tau_{on} \sim \mathcal{N}(0,\ 5)$$

$$\tau_{off} \sim \mathcal{N}(0,\ 200)$$

$$\sigma \sim |\mathcal{N}(0,\ 1)|$$

The likelihood of the model was subsequently defined in terms of a normal distribution centered according to:

$$\mathcal{L}(A(\beta,f))\ |A \sim \mathcal{N}(A(t;\beta,f),\ \sigma)$$

Transformation of trigeminal activity in Rh5/6

To express the activity in this hindbrain region in terms of the activity of trigeminal cell-types we used a filter-parametrization that would allow for integrating as well as differentiating filters:

$$\mathrm{f}(\Delta\mathrm{t};\mathrm{s},\hat{\mathrm{o}}_1,\tau_2) = s\Delta t e^{-\frac{\Delta t}{\tau_0}} + (1-\Delta t)e^{-\frac{\Delta t}{\tau_1}}\ |-4\mathrm{s} \le \Delta t \le 0$$

To simplify computation, convolution in the model was again expressed via piecewise multiplications such that the predicted output activity A(t) of a cell type in Rh5/6 was described in terms of the input activities ON(t) and OFF(t) as:

$$A(t;\beta_{ON},\ \beta_{OFF},\ f) = \beta_{ON}\sum_{\Delta t} ON(t-\Delta t)f(\Delta t) + \beta_{OFF}\sum_{\Delta t} OFF(t-\Delta t)f(\Delta t)\ |-4s \le \Delta t \le 0$$

Since trigeminal neurons are largely glutamatergic, we enforced all trigeminal inputs to have activating effects in our models. However, to express the Fast-ON, Fast-OFF and Delayed-OFF types in terms of their inputs required inhibition. Those Rh 5/6 types were therefore expressed in terms of a strictly activating trigeminal input and a potentially inhibitory input from either the Slow-ON or Slow-OFF type. The prior distributions of β reflected this constraint:

Slow-ON, Slow-OFF

$$\beta_{ON} \sim |\mathcal{N}(0,\ 2)|$$

$$\beta_{OFF} \sim |\mathcal{N}(0,\ 2)|$$

Fast-ON, Fast-OFF

$$\beta_{ON} \sim |\mathcal{N}(0,\ 2)|$$

$$\beta_{OFF} \sim \mathcal{N}(0,\ 2)$$

Delayed OFF

$$\beta_{ON} \sim \mathcal{N}(0,\ 2)$$

$$\beta_{OFF} \sim |\mathcal{N}(0,\ 2)|$$

The priors of the remaining parameters were shared between all models:

$$\tau_1 \sim |\mathcal{N}(0,\ 10)|$$

$$\tau_2 \sim |\mathcal{N}(0,\ 10)|$$

$$s \sim |\mathcal{N}(0,\ 5)|$$

$$\sigma \sim |\mathcal{N}(0,\ 1)|$$

The likelihood of the model was subsequently defined in terms of a normal distribution centered according to:

$$\mathcal{L}(A(\beta_{ON},\ \beta_{OFF}, f))\ |A \sim \mathcal{N}(A(t; \beta_{ON}, \beta_{OFF}, f),\ \sigma)$$

Rate coding steps

The last two stages of the model were implemented as simple linear regression steps relating the weighted sum of input activity to output activity.

$$A_{out}(\beta) = A_{in}\beta^T$$

The prior distributions on the parameters β and the error standard deviation σ were defined as:

$$\beta_i \sim \mathcal{N}(0,\ 2)$$

$$\sigma \sim |\mathcal{N}(0,\ 1)|$$

And the model likelihood was expressed according to:

$$\mathcal{L}(A(\beta))\ \ |A \sim \mathcal{N}(A_{out}(\beta),\ \sigma)$$

Simulation of filter derivation

To test the influence of noise in our data on filtering, a simple simulation was performed. The temperature stimulus T(t) was used as the input to a sharp high pass filter (Figure S5I, orange line) to create the discrete difference trace δT(t) of the temperature stimulus:

$$\delta T(t) = T(t) - T(t-1)$$

Both the original temperature trace and the difference trace were subsequently corrupted by i.i.d. Gaussian noise:

$$I(t) = T(t) + \epsilon(t)\ \ |\epsilon(t) \sim \mathcal{N}(0,\ 0.2)$$

$$O(t) = \delta T(t) + \epsilon(t)\ \ |\epsilon(t) \sim \mathcal{N}(0,\ 0.2)$$

These traces were subsequently used as inputs and outputs to derive a model using the same filter parametrization and strategy as above for cell types in Rhombomeres 5 and 6. As can be seen in Figure S5I, the derived filter (black trace) extends over considerably longer timescales than the true differencing filter (orange trace).

QUANTIFICATION AND STATISTICAL ANALYSIS

All data analysis was performed in python.

All confidence intervals and standard errors displayed in figures are derived using bootstrapping across cells and appropriate n-values are indicated in the figure legend. As indicated in the figure legends bootstrap hypothesis testing was used to determine significance testing except in the case of trigeminal ablations where a nonparametric ranksum test was used across 3 fish to assess significance. Counts either refer to cells or individual fish as indicated in the figure legends where applicable.

Data shuffles

Since the stimulus presented on each imaging plane is repeated three times, cell activity that reflects the stimulus should follow the same repeat structure. The data shuffles used for the analysis of heat modulated cells in Figures S1D–S1E and S4E–S4F were therefore generated as follows. Each cell's activity trace was split into the three repeats and each repeat was independently circularly permuted. This should break the repeat structure but leave in-repeat timescale structures intact. The activity generated this way was subsequently subjected to the same whole-brain or regional clustering approaches detailed above.

Since regression-based analysis was used to identify motor-correlated cells a different approach was used to create the controls in Figure S3A–S3C. In this case the whole activity trace of a cell was circularly permuted with respect to the motor regressors again keeping the overall structure of the activity data intact. The shuffled activity was subsequently probed with the motor regressors as described above.

DATA AND SOFTWARE AVAILABILITY

Raw experimental data (~40 GB) and custom written analysis as well as acquisition software will be made available by the authors upon request.